



## Invited review

## Degradation of solid oxide electrolysis cells: Phenomena, mechanisms, and emerging mitigation strategies—A review

Yi Wang<sup>a</sup>, Wenyuan Li<sup>a</sup>, Liang Ma<sup>a,b</sup>, Wei Li<sup>a</sup>, Xingbo Liu<sup>a,\*</sup><sup>a</sup> Department of Mechanical & Aerospace Engineering, West Virginia University, Morgantown, WV, 26506-6106, USA<sup>b</sup> School of Materials Science and Engineering, Hebei University of Engineering, Handan 056038, China

## ARTICLE INFO

## Article history:

Received 19 February 2019

Received in revised form 7 May 2019

Accepted 20 May 2019

Available online 24 July 2019

## Keywords:

Solid oxide electrolysis cell

Degradation

Electrode/electrolyte interface

Mitigation

Strategy

## ABSTRACT

Solid oxide electrolysis cell (SOEC) is a promising electrochemical device with high efficiency for energy storage and conversion. However, the degradation of SOEC is a significant barrier to commercial viability. In this review paper, the typical degradation phenomena of SOEC are summarized, with great attention into the anodes/oxygen electrodes, including the commonly used and newly developed anode materials. Meanwhile, mechanistic investigations on the electrode/electrolyte interfaces are provided to unveil how the intrinsic factor, oxygen partial pressure  $p_{O_2}$ , and the electrochemical operation conditions, affect the interfacial stability of SOEC. At last, this paper also presents some emerging mitigation strategies to circumvent long-term degradation, which include novel infiltration method, development of new anode materials and engineering of the microstructure.

© 2019 Published by Elsevier Ltd on behalf of The editorial office of Journal of Materials Science & Technology.

## Contents

1. Introduction.....	35
2. Degradation phenomena of SOECs .....	36
2.1. Oxygen electrode degradation .....	37
2.1.1. Degradation of LSM oxygen electrode .....	37
2.1.2. Degradation of LSCF oxygen electrode .....	39
2.1.3. Degradation of newly developed oxygen electrodes .....	41
2.2. Electrolyte degradation .....	44
2.3. Hydrogen/cathode degradation .....	45
3. Status of electrode/electrolyte interfaces governed by $p_{O_2}$ .....	47
4. Emerging mitigation strategies and proton-conducting SOEC .....	50
5. Concluding remarks .....	53
Acknowledgements .....	53
References .....	53

## 1. Introduction

In recent decades, there has been a growing concern about the massive use of finite fossil fuels such as coal, petroleum, and natural gas, which greatly contributes to the CO<sub>2</sub> emission [1–4]. The ever-increasing CO<sub>2</sub> in the atmosphere is considered to be responsible for global warming and environmental destruction [5,6]. In the

meanwhile, the recent boom in solar, wind power and tidal renewable energy development provides a variety of power sources to be utilized in large scales [7,8]. Solid oxide electrolysis cell (SOEC) as a strategic technology that can collectively connect these renewable energy sources to the insatiable demand for fuel and power through its eco-friendly, high efficient electricity-fuel conversion ability, shows the profound impact on social benefit and economical advantage [9–17].

A typical oxygen-conducting SOEC consists of a porous anode, a dense electrolyte and a porous cathode with a “sandwich” structure, as shown in Fig. 1 [5,18]. The cathode side is fed with a

\* Corresponding author.

E-mail address: [Xingbo.liu@mail.wvu.edu](mailto:Xingbo.liu@mail.wvu.edu) (X. Liu).

gas stream composed of either  $\text{H}_2\text{O}$ ,  $\text{CO}_2$  or their mixture that is reduced to  $\text{H}_2$ ,  $\text{CO}$  or syngas fuel. Then, the dissociated oxygen ions are transported from the cathode side to the anode through the dense electrolyte, driven by an external voltage that is higher than the Nernst potential. Oxygen ions are finally oxidized to oxygen molecules in the anode, accompanied by electron releasing. SOEC features a number of advantages as an electrochemical device: [9] (1) the production of hydrocarbon fuels from  $\text{CO}_2$ , water, and renewable electricity can be used as transportation fuels; (2) the process is precise and easy to control by controlling the electrode potentials and reaction temperatures; (3) the conversion systems are compact, modular, on-demand, and scalable; and (4) the process can utilize clean energy sources such as solar, wind, geothermal, tidal, etc., as well as surplus electricity from nuclear and hydroelectric sources [6,19].

The high efficiency of SOEC can be attributed to the high operating temperature. As seen in Fig. 2 [13], the total energy needed ( $\Delta H$ ), is nearly constant from room temperature up to  $1200^\circ\text{C}$ , for both  $\text{CO}_2$  and steam electrolysis. In contrast, the total electrical energy consumption ( $\Delta G$ ) decreases with the increasing temperature. The energy difference is compensated by increasing heat supply ( $T\Delta S$ ). Considering the lower cost of heat than electricity, high temperature electrolysis is more economically favored. From the kinetic point of view, high temperature also benefits the system by ensuring high electrode activity towards related electrochemical reactions. According to Lamy [20], the electrical energy efficiency of a SOEC operated at  $800^\circ\text{C}$  can reach 60%–70% depending on the working conditions.

To facilitate the commercialization of SOEC, extensive investigations have been implemented to develop the materials. The electrode materials offer active sites for electrochemical reactions: reduction of  $\text{H}_2\text{O}$  and  $\text{CO}_2$  in the cathode and oxygen evolution reaction (OER) in the anode side. Also, the electrode materials provide paths for reactants, products and electrons transport. The electrolyte accommodates the transport of oxygen ions, which dominates the cell's ohmic resistance. Ni-based cermet is a commonly used cathode because of its high catalytic activity, chemical and thermal compatibility with electrolytes. However, the deactivation by coking and Ni oxidation prevents its application in  $\text{CO}_2$  electrolysis. In this case, ceramic mixed ionic and electronic conductors (MIECs) are popular alternatives because of their record-proven stability in the  $\text{CO}_2$ -containing atmosphere, such as doped  $\text{LaCrO}_3$ , double perovskite  $\text{Sr}_2\text{Fe}_{1.5}\text{Mo}_{0.5}\text{O}_6$  and  $\text{La}_x\text{Sr}_{1-x}\text{TiO}_{3+\delta}$  etc. For the electrolyte, yttrium stabilized zirconia (YSZ), gadolinium doped ceria (GDC) and strontium and magnesium doped lanthanum gallate (LSGM) are usually electrolytes of choice. For anode material, perovskites, Ruddlesden-Popper (RP) phase oxides and double-perovskite oxides are key players, among which lanthanum strontium manganite (LSM) based materials and “La–Sr–Co–Fe” system such as  $\text{La}_{0.6}\text{Sr}_{0.4}\text{Co}_{0.2}\text{Fe}_{0.8}\text{O}_3$  (LSCF) are the most commonly investigated anode materials. There have been several previous reviews [1,2,5,6] that summarize the development of materials for electrodes and electrolytes.

Up to date, though the initial performance of SOECs based on these materials is promising, the long-term stability is of great concern. It was reported that the long-term testing of a Ni/YSZ-supported single cell with YSZ electrolyte and LSCF air electrode demonstrated a 2.26%/kh–5.62%/kh degradation rate under a 900 h measurement [21]. The degradation rates of a 5 Ni/YSZ supported SOEC stack and a 10 electrolyte-supported cell stack made by commercial companies with 1 kh or longer operation were approximately 3.2%/kh and 4.6%/kh, respectively [22]. A lower degradation rate of SOEC, 1.7%/kh for 3.6 kh operation, was reported by Schefold et al [23]. However, a degradation rate of  $\sim 1\%$ /kh or lower is required for the commercialization of SOEC stacks for high-temperature

electrolysis, proposed by Idaho National Laboratory [22], similar to the requirement for SOFC commercialization [11,24].

Because of the significance of understanding the degradation of SOEC, Jiang [25] and Chen et al. [26] reviewed the durability and performance degradation of SOECs with emphasis on the material properties from the compositional and microstructural perspectives. The review paper of Moçoteguy and Brisse [27] focused more on the principal investigations of SOEC degradation by incorporating mass transport theory and electro-catalytic kinetics. In the present review work, we focus on providing an understanding of SOEC degradation from the perspective of the local distribution of oxygen partial pressure ( $p_{\text{O}_2}$ ) or oxygen chemical potential ( $\mu_{\text{O}_2}$ ), which is an overarching factor governing various degradation phenomena including cation diffusion, secondary phase formation and delamination of electrode. This review aims to provide readership clear mechanistic understanding of the role of  $p_{\text{O}_2}$  (or  $\mu_{\text{O}_2}$ ) distribution in the stability of SOEC and to inspire more research endeavour and new strategies to mitigate the SOEC deterioration.

In this work, we first summarize the degradation phenomena of SOECs and the proposed mechanisms, with special attention paid to the degradation in the air electrode (anode) side, such as anode delamination and electrolyte disintegration, since the anode was found the major source of degradation, particularly in the steam electrolysis. Meanwhile, mechanistic works unveiling the different principles between SOEC and SOFC are presented to evaluate the faster degradation of SOEC than SOFC, in which the focus is the distribution of  $p_{\text{O}_2}$  (or  $\mu_{\text{O}_2}$ ). At last, newly presented counter strategies against the degradation of SOEC are also provided, which include the novel infiltration, new anode materials and microstructure engineering.

## 2. Degradation phenomena of SOECs

The stability of a SOEC depends upon cell materials, fabrication procedure and operating conditions [27] which include operating temperature, current density or cell polarization and feed gas (composition and purity) [28]. For example, Ni-based cathode suffers coking in  $\text{CO}_2$  electrolysis and Ni depletion at the vicinity of the interface in steam electrolysis. LSCF anode would be subject to severe inter-diffusion in high-temperature because of the agility of Sr and Co. Under low electrolysis current, LSM anode incorporates excess oxygen in the lattice, inducing the shrinkage and crack of LSM particles [29], while under the higher current or polarization, La is driven to react with Zr forming insulating  $\text{La}_2\text{Zr}_2\text{O}_7$  phase [30,31]. Contaminants and impurities such as silicon, chromium and sulfur can also cause damage to the cell components.

Behind these cell degradation phenomena, the  $p_{\text{O}_2}$  (or  $\mu_{\text{O}_2}$ ) across the whole cell, especially in the electrode/electrolyte interfaces, seems to be a predominant and intrinsic factor. Firstly, oxygen participates in nearly all parasitic reactions so that the  $p_{\text{O}_2}$  can strongly affect the Sr segregation forming SrO on the surface, the generation of detrimental secondary phases  $\text{SrZrO}_3$  or  $\text{La}_2\text{Zr}_2\text{O}_7$ , and the anode delamination. Second, the  $p_{\text{O}_2}$  determines the chemical stability and catalytic ability of oxide materials in the SOEC system. If the  $p_{\text{O}_2}$  is lower than the critical value, the material would decompose because the lattice structure would collapse if lacking oxygen. The  $p_{\text{O}_2}$  influences the catalytic capability because the electronic density of states (DOS) of MIECs is partially contributed from oxygen ( $\text{O } 2p$ ) [32]. Besides, the  $p_{\text{O}_2}$  can affect the ionic and electronic conductivity of electrode and electrolyte materials. For example, the loss of lattice oxygen in  $\text{La}_{1-x}\text{M}_x\text{Co}_{1-y}\text{Fe}_y\text{O}_{3-\delta}$  ( $\text{M} = \text{Sr}, \text{Ba}, \text{Ca}$ ) perovskites increases the oxygen flux and decreases the electronic conductivity at high temperature [33].

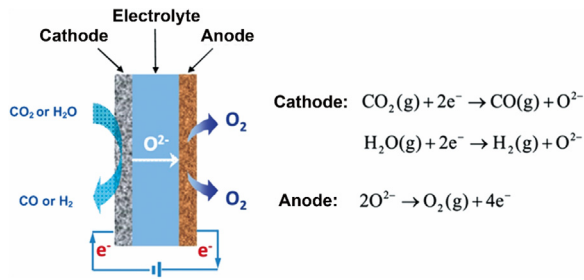


**Fig. 1.** [5] A typical schematic of SOEC and the reaction paths for CO<sub>2</sub> and H<sub>2</sub>O electrolysis based on oxygen ion conducting electrolyte. Reproduced with permission from ref 5. Copyright 2017 Elsevier, Inc.

Consequently, in what follows, the typical degradation phenomena of all components and the related mechanisms will be presented, in which the role of  $p_{O_2}$  would be comprehensively examined. Because the oxygen electrode contributes a major part to the whole degradation, the main body of this section would be the discussion of anode stability, including LSM, LSCF and newly developed anode materials.

### 2.1. Oxygen electrode degradation

In terms of the contribution of different components of SOEC to the whole cell degradation, Graves et al. [34] found that at lower current density operation (0.25 A/cm<sup>2</sup>) the degradation of the cathode electrode was dominant, while at higher current densities (0.5 A/cm<sup>2</sup> and 1 A/cm<sup>2</sup>), the cathode continued to degrade but the degradation of oxygen electrode began to play a major role [34]. In fact, SOEC with high current density operation is preferred in the view of practical application. The exploration of SOEC cell and stack technology with ultra-high steam electrolysis current (>3 A/cm<sup>2</sup>) is ongoing in the US for potentially ultra-low-cost, high-efficient hydrogen production from diverse renewable sources [35]. In this context, the stability of anode is of great significance.

LSM and LSCF are the most commonly used oxygen electrode materials. LSM is mainly used in high-temperature SOEC, typically 800–900 °C, due to its acceptable performance and chemical and thermal stability. LSCF is usually applied in the intermediate-temperature because it still shows good oxygen diffusivity and oxygen exchange coefficient at relatively low temperature. However, performance degradation caused by delamination, cation diffusion and the formation of detrimental secondary phase had been observed during the practical operation of the LSM and LSCF based SOECs.

#### 2.1.1. Degradation of LSM oxygen electrode

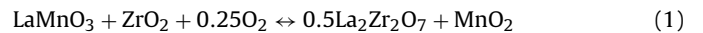
For LSM-based SOEC oxygen electrode, delamination is a severe degradation type that is often observed, as seen in Fig. 3 [29,31]. Fig. 3(a) and (b) shows the anode of tested and non-operated LSM||YSZ||LSM symmetric cells, respectively. The anode delaminated from YSZ electrolyte after electrolysis test [31]. Fig. 3(c) and (d) exhibits the microstructure of the cross-section of the LSM/YSZ interface before and after anodic polarization [29]. Momma et al. [36] ascribed this phenomenon to the high  $p_{O_2}$  established in the closed pores existing in the anode/electrolyte interface during electrolysis operation.

Additionally, the delamination can be attributed to the localized disintegration of the LSM grains and the formation of nanoparticles at the electrode/electrolyte interface [29]. As seen in Fig. 4 [29], Fig. 4(a) presents the YSZ surface in contact with LSM electrodes before polarization. The LSM coating was removed by HCl treatment. Fig. 4(b) and (c) show the YSZ surface after the anodic current passage at 0.5 A/cm<sup>2</sup> and 800 °C for 48 h before and after

acid treatment, respectively. Compared with the “fresh” YSZ surface in Fig. 4(a), the YSZ surface after anodic polarization in Fig. 4(b) shows clusters consisting of nanoparticles originated from the LSM electrode since they can be dissolved by an acid solution. Based on the distinct phenomenon, the proposed mechanism of delamination is illustrated in Fig. 4(d)–(i): (d) oxygen transport from YSZ electrolyte to LSM grain bulk at the interface which is facilitated by the anodic polarization and high electrochemical potential of oxygen ions, (e) the formation of local tensile strain because the LSM lattice would shrink by the incorporation of excess oxygen and the consequent increase of Mn ions valence and the cation vacancies, (f) local tensile strains induced microcrack, (g) formation of individual particles, (h) propagation and continuous formation of nanoparticles and the increase of pressure due to the formation of oxygen gas, (i) complete nanoparticles formation and the occurrence of delamination.

Delamination is accompanied by the formation of La<sub>2</sub>Zr<sub>2</sub>O<sub>7</sub>, when SOEC is operated under the high current load (or high polarization) [31]. Fig. 5(a)–(d) shows the SEM images of YSZ electrolyte surfaces of LSM||YSZ||LSM symmetric cells after the HCl acid treatment to remove the LSM electrodes, each of which was tested at different voltages at 840 °C for 100 h: (a) OCV, (b) 0.3 V, (c) 0.5 V, (d) 0.8 V. It was obvious that the LSM/YSZ interface underwent severe morphological and chemical changes: the broadening ridge, porosity formation in the grain boundary, lanthanum zirconate particles formation and delamination of electrode. The higher the polarization, the higher the severity of the chemical change. On the basis of the post-mortem characterization, detailed description of the mechanism for this kind of delamination was provided, as seen in Fig. 5(e)–(h) [31].

La<sub>2</sub>Zr<sub>2</sub>O<sub>7</sub> formation at the anode/electrolyte interface can be ascribed to the following reaction (strontium is excluded for simplicity) [31,37]:



The Gibbs free energy of the reaction is shown as follows:

$$\Delta G = \Delta G^0 + RT \ln \left( \frac{a_{\text{LZ}}^{0.5} a_{\text{MO}}}{a_{\text{LM}} a_{\text{ZO}} a_{\text{O}}^{0.25}} \right) \quad (2)$$

where,  $\Delta G^0$  is the standard Gibbs free energy,  $R$  is the gas constant,  $T$  is the temperature, and  $a_i$  in parentheses are the activities of the species  $i$  in the reaction, where LZ is denoted to La<sub>2</sub>Zr<sub>2</sub>O<sub>7</sub>, LM is LaMnO<sub>3</sub>, ZO is ZrO<sub>2</sub>. According to the data from Chen [37], the  $\Delta G$  would be negative at  $p_{O_2}$  greater than 3.7 atm, which means that in the high partial pressure, the formation of La<sub>2</sub>Zr<sub>2</sub>O<sub>7</sub> is favourable.

More distinct characteristics of LSM anode degradation can be observed at even higher current passage, such as densification of LSM. Fig. 6(a) and (b) demonstrates the interfaces of both electrode sides of the LSM/YSZ||YSZ||LSM/YSZ symmetric cell which was operated at 1.5 A/cm<sup>2</sup> for 120 h at 750 °C in the air [30]. On the cathode sides, the LSM electrode does not suffer noticeable change; however, for the anode, significant densification occurs in some parts of the LSM electrode where pores are eliminated, and thickness is reduced. Also, delamination of LSM anode, the formation of pores along the YSZ grain boundaries near the interface and intensive inter-diffusion of LSM and YSZ can be found in Fig. 6(c) and (d). The authors [30] attributed these degradation phenomena to the severe cation migration between LSM and YSZ, which was facilitated by anodic polarization. The primary pathway for cation transport is through prevailing point cationic defects in the cationic sublattice. When under cathodic current load, the concentration of cation vacancies would be reduced and thus the mobility of cation would decrease either, and this leads to the suppressed sinterability of LSM [38,39]. However, the cationic vacancy in LSM tends to increase because of the oxidative condition when loaded by

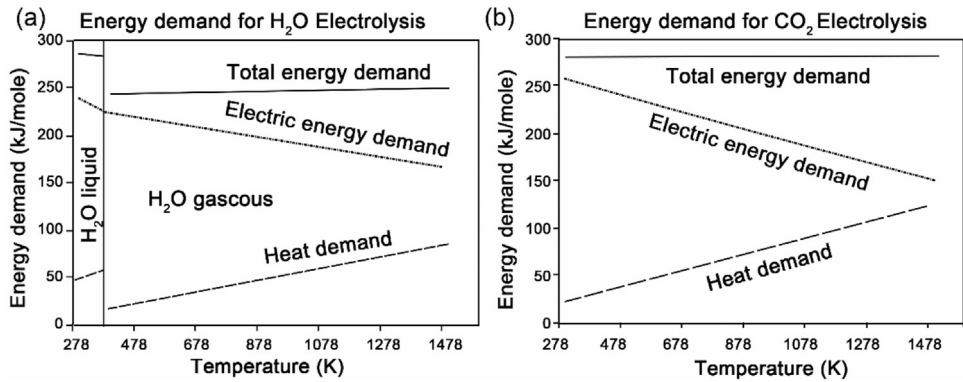


**Fig. 2.** [13] Thermodynamics of steam and carbon dioxide electrolysis. Both steam and CO<sub>2</sub> electrolysis become increasingly endothermic with temperature increasing. Reproduced with permission from ref 13. Copyright 2007 Elsevier, Inc.

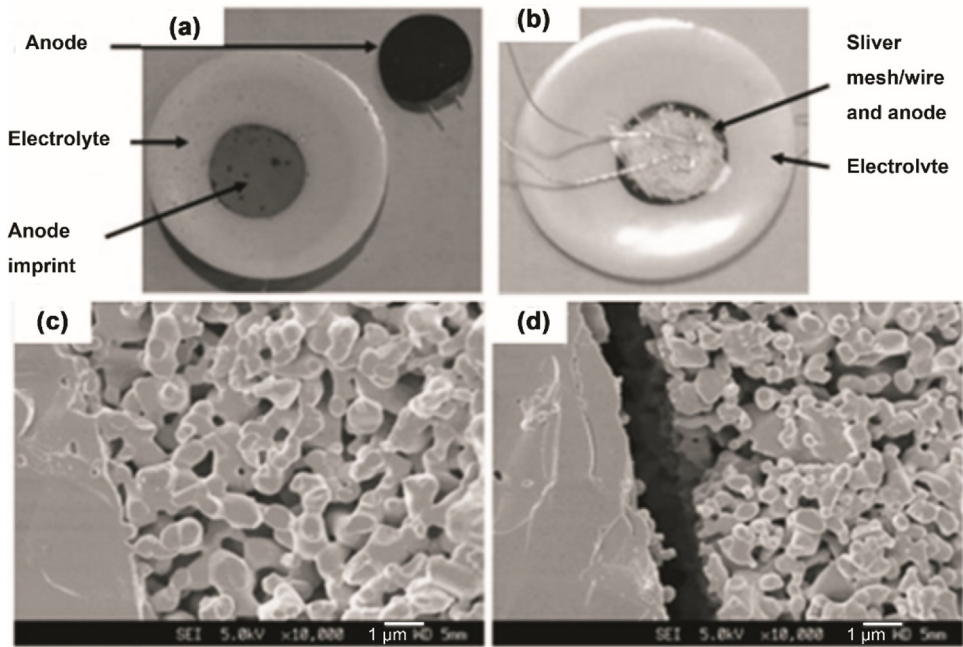
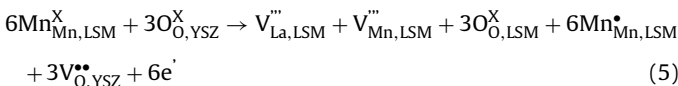
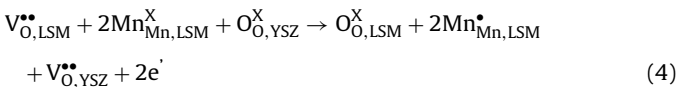
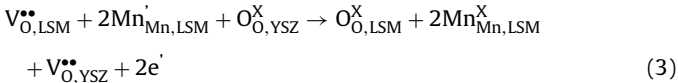


**Fig. 3.** [29,31] Photographs of two identical LSM/YSZ/LSM symmetric cells under operation or non-operation: (a) LSM anode delaminates from YSZ electrolyte after anodic operation for 100 h at 0.8 V, (b) the anode remains intact of the untested symmetric cell [31]. Reproduced with permission from ref [31]. Copyright 2012 Elsevier, Inc. SEM images of the cross-section of the LSM oxygen electrode / YSZ electrolyte interface (a) before and (b) after anodic polarization at 0.5 A/cm<sup>2</sup> and 800 °C for 48 h [29]. Reproduced with permission from ref [29]. Copyright 2011 Elsevier, Inc.

the anodic current, then facilitating the cationic mobility and LSM sinterability [40]. In addition, the existence of an external electrical field on multi-component oxides is the driving force for cation motion, because the electrical field can induce defect fluxes that leads to cation fluxes [41,42]. The kinetic demixing promotes the cation migration, and then facilitates the enhanced sinterability of the LSM electrode. Below are the deactivation reactions under anodic polarization [38], which are the reverse processes of activation of LSM under cathodic current.



Cr poisoning also happens to SOECs [43–45]. Fig. 7 (a)–(c) shows the distribution of Mn, Co and Cr in an LSM electrode from a SOEC stack operated at 830 °C for 1000 h [44]. The lighter shades of gray indicate a greater elemental abundance. In addition to the obvious inter-diffusion between Mn and Co, Cr also deposits in the electrode, particularly along the edges near the gas seals. The depth profile of Cr is also presented in Fig. 7 (d), where the lighter shades correspond to greater buried element abundance. It is clear that Cr migrated deeper towards the electrolyte interface, leading to the higher possibility of degradation by Cr substitution into perovskite B-sites, SrCrO<sub>4</sub> formation and Cr<sub>2</sub>O<sub>3</sub> or spinel CrMn<sub>2</sub>O<sub>4</sub> formation [44].

The detrimental effect of boron deposition and poisoning on the LSM anode was observed by Chen et al [46]. The presence of volatile boron species greatly degraded the electrode activity for OER, impaired the chemical stability and microstructure of LSM anode, and accelerated the delamination [46]. During electrolysis operation, boron deposition preferen-



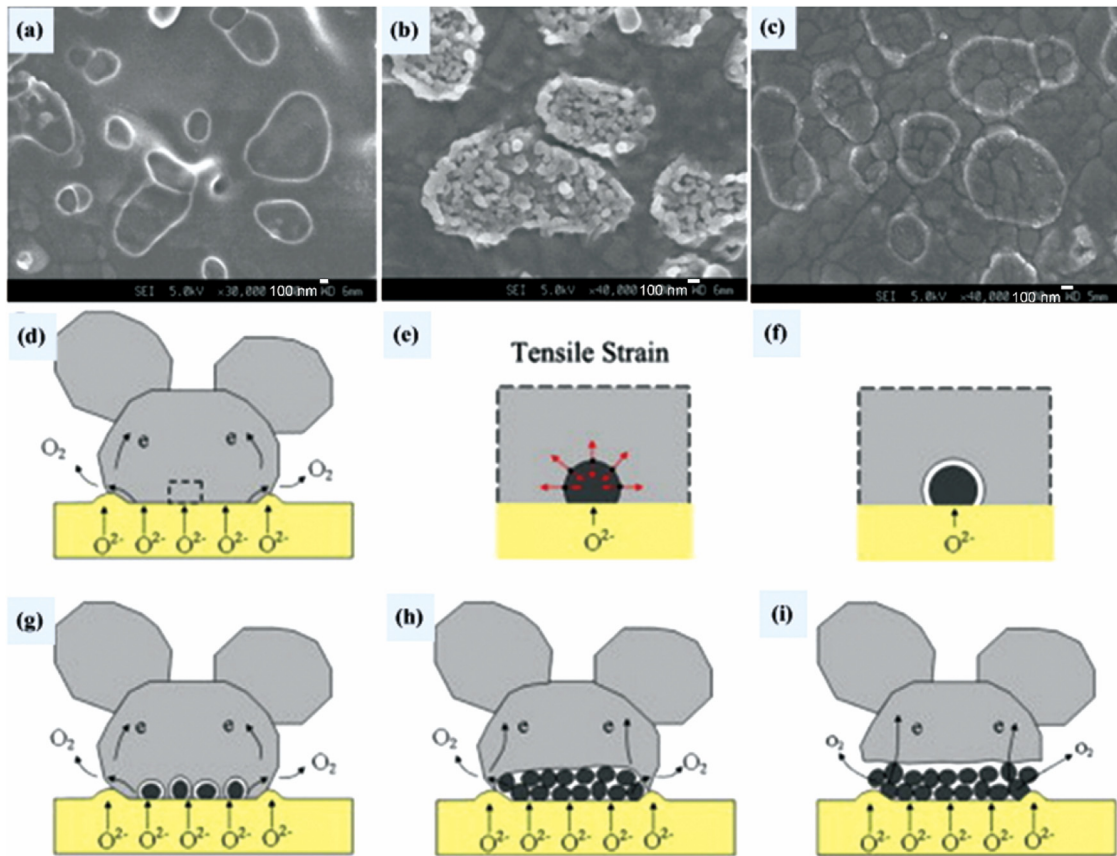


**Fig. 4.** [29] (a) The YSZ electrolyte surface in contact with the LSM electrode before the polarization. LSM coating was removed by HCL treatment. (b) and (c) show the YSZ surface after the anodic current passage at  $0.5 \text{ A/cm}^2$  and  $800^\circ\text{C}$  for 48 h before and after acid treatment, respectively. (d)–(i) show schematic illustrations of the microstructural change of the LSM oxygen electrode/YSZ electrolyte interface under SOEC operation conditions. Reproduced with permission from ref [29]. Copyright 2011 Elsevier, Inc.

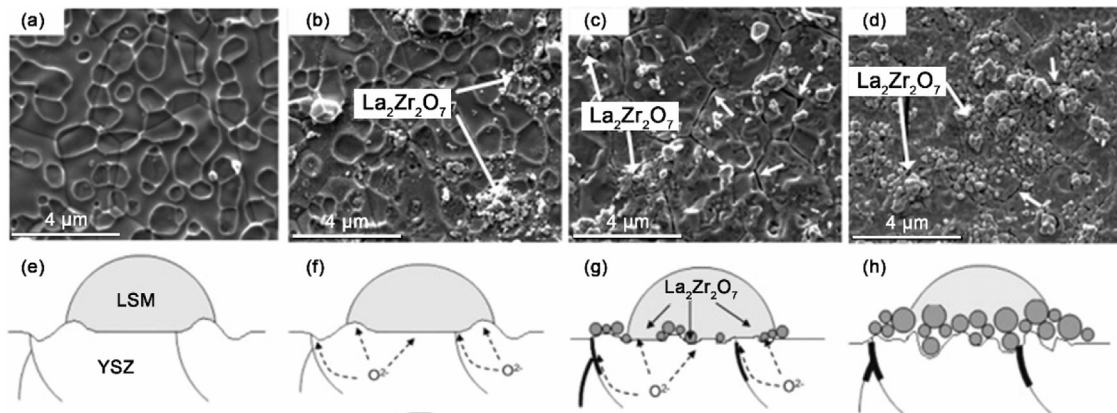


**Fig. 5.** [31] SEM images of YSZ electrolyte surfaces of LSM-YSZ-LSM symmetry cells after HCl acid treatment to remove the LSM electrodes, each of which was tested at different voltages at  $840^\circ\text{C}$  for 100 h: (a) OCV, (b) 0.3 V, (c) 0.5 V, (d) 0.8 V. Proposed mechanism (e)–(h): (e) YSZ ridge forms at triple-phase boundary due to surface cation migration [132,133] when LSM electrode is as-sintered on YSZ surface, (f) oxygen ions diffuse through YSZ bulk and grain boundaries in the initial stage of voltage application, (g)  $\text{La}_2\text{Zr}_2\text{O}_7$  forms at the anode-electrolyte interface and porosity forms in the electrolyte grain boundaries when the voltage continues, (h) porosity enhances in the electrolyte grain boundaries and  $\text{La}_2\text{Zr}_2\text{O}_7$  particles form fully coverage on the YSZ electrolyte that intensively weakens the interface and causes delamination at the end of electrical testing. Reproduced with permission from ref [31]. Copyright 2012 Elsevier, Inc.

tially took place in the LSM/YSZ interface region, resulting in the formation of lanthanum borates and manganese oxides [46]. Sulfur poisoning was studied by Wang et al. [47], it was found that Sulphur deposition tended to occur at the LSM/YSZ interface and the inner layer of LSM electrode, leading to the formation of  $\text{SrSO}_4$ .

### 2.1.2. Degradation of LSCF oxygen electrode

Because of the excellent electrical and catalytic performance,  $\text{LaCoO}_3$ -based materials, such as LSCF was proposed to be used as the air electrode at intermediate-temperature [12]. Usually, a GDC barrier layer is inserted between the YSZ electrolyte and the LSCF anode to prevent the formation of detrimental phases such

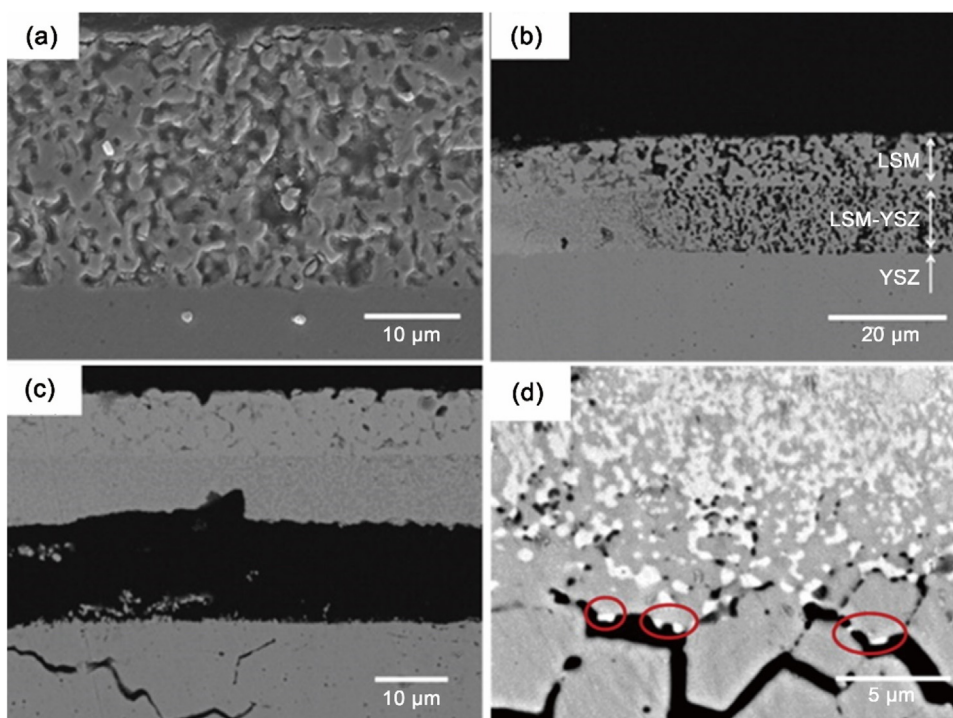


**Fig. 6.** [30] SEM images of LSM-YSZ interface after 1.5 A/cm<sup>2</sup> current passage for 120 h at 750 °C in air (a) the cathode (b) the anode. (c) The delamination of anode electrode from the electrolyte. (d) Interface area between LSM/YSZ electrode and YSZ electrolyte. Reproduced with permission from ref [30]. Copyright 2013 Elsevier, Inc.

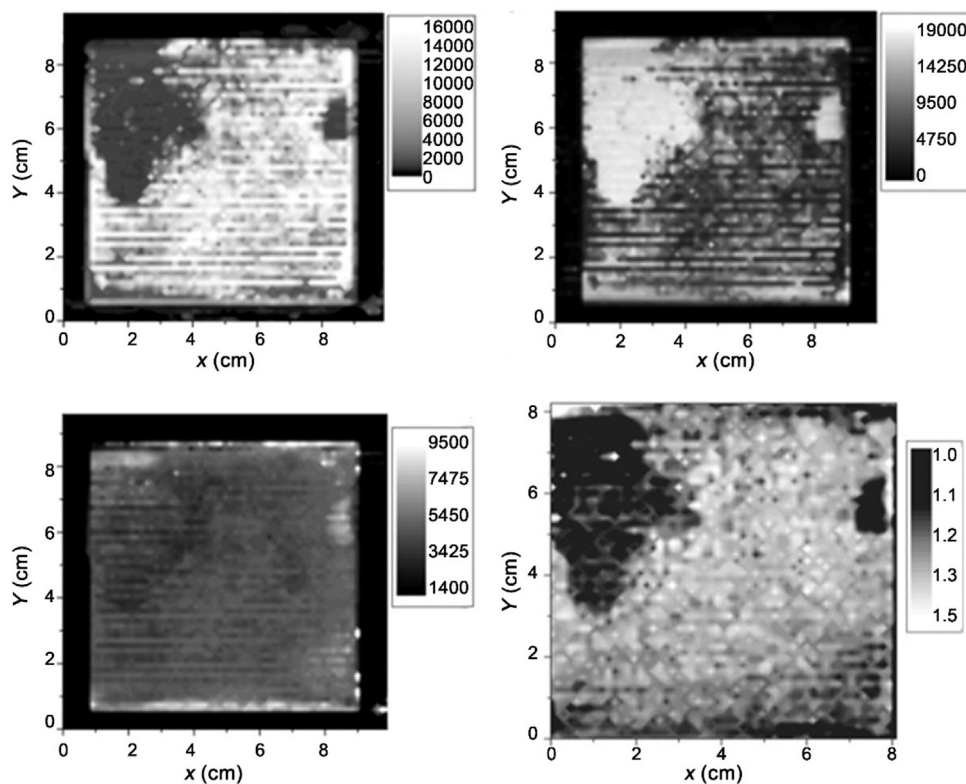


**Fig. 7.** [44] X-ray fluorescence maps of (a) Mn, (b) Co and (c) Cr abundance in the oxygen electrode of a 1000-h cell. Lighter shading corresponds to a greater concentration of the element. The sealed edges were along the top and bottom edges of the cell. (d) Cr in the 1000-h oxygen electrode. Darker shading corresponds to more of the element near the surface and lighter shading corresponds to greater buried element abundance. Oxygen flowed over the electrode from right to left. Reproduced with permission from ref [46]. Copyright 2009 Elsevier, Inc.

as SrZrO<sub>3</sub> and La<sub>2</sub>Zr<sub>2</sub>O<sub>7</sub>. However, LSCF-based SOEC also degrades during the SOEC operation. Schefold et al. [11,23,48–51] studied the long-term stability of different SOECs with the LSCF anode, all showing continuous degradation. A Ni/YSZ supported cell shows a degradation rate of 3.8%/kh under 1 A/cm<sup>2</sup> anodic current load at 778 °C [51].

The major degradation phenomenon regarding the LSCF air electrode is the severe cation diffusion and the formation of SrZrO<sub>3</sub> [24,52–55]. Mahmoud et al. [54] observed the formation of Co<sub>3</sub>O<sub>4</sub> resulting in partial structure decomposition of LSCF and the detrimental phase SrZrO<sub>3</sub> formation in the anode/electrolyte interface, as well as the valence reduction of iron from Fe<sup>4+</sup> to Fe<sup>3+</sup> in LSCF, after a long-term SOEC operation which showed steady deterioration. Frey et al. [55] tested a LSCF-based SOEC stack for more than 20 kh. The demixing of the air electrode led to the segregation of strontium, which was visible in the formation of SrZrO<sub>3</sub> at the interface between the electrolyte and the GDC barrier layer as well as in the formation of strontium oxide and strontium chromate on top of the cells [55], as seen in Fig. 8.

Laurencin et al. [24] carried out a set of long-term tests (>1 kh) on typical Ni/YSZ||YSZ||GDC||GDC/LSCF cells in fuel cell and electrolysis cell modes, to investigate the effect of the SOFC versus SOEC polarizations on the electrochemical degradation rate of a typical LSCF/GDC composite anode. Fig. 9 shows SEM-EDX images of interfaces in anode side (a) for the pristine cell, (b) for cell operated in SOFC mode and (c, d) for cell operated in SOEC mode [24]. It was seen that under anodic polarization, Sr diffused across the GDC layer and reached the GDC/YSZ interface, while under cathodic current load, no Sr diffusion could be observed [24]. The diffusion of Co into the GDC/YSZ interface was also observed, suggesting the degradation of LSCF electrode, since Co is a B-site element that significantly enhances the electrocatalytic ability of LSCF electrode.

The authors ascribed it to the combined effects of the anodic electric field and high  $p_{O_2}$  [24]. The electrical field gradient in electrolysis is against the Zr<sup>4+</sup> cations diffusion from the electrolyte toward the GDC barrier layer, however can accelerate the diffusion of Sr<sup>2+</sup> into the GDC/YSZ interface. Meanwhile, the high  $p_{O_2}$  would decrease the oxygen vacancy concentration in LSCF, driving the demixing and the SrO precipitation:



However, there are discrepancies concerning the role of polarization in the Sr segregation. Ai et al. [56] and He et al. [57] found that the formation of SrZrO<sub>3</sub> and Sr segregation is suppressed by the anodic polarization when using directly assembled LSCF-based oxygen electrodes on barrier-layer-free YSZ electrolyte of SOECs. They suggested that surface oxygen vacancies decrease under the anodic polarization conditions, resulting in a reduced driving force for the reaction between Sr<sup>2+</sup> and oxygen vacancies and therefore a limited Sr surface segregation.

The mechanisms of cation diffusion of the LSCF/GDC/YSZ interfaces have been extensively studied by De Vero et al. [52,58,59]. It was found that under OCV, SrZrO<sub>3</sub> laterally formed at the O<sub>2</sub>/LSCF/GDC triple phase boundary with GDC interlayer showing increased porosity near the YSZ electrolyte, as seen in Fig. 10(a). However, under cathodic polarization, localized transverse growth of SrZrO<sub>3</sub> was observed, and pores were apparently eliminated in GDC. In addition to that, the microstructure of LSCF can affect GDC stability and cation diffusion [52]. The interdiffusion and microstructural evolution of a porous LSCF made by screen-printing and a dense LSCF made by pulsed laser deposition were investigated at temperatures of 800 °C–1000 °C in the air. At 1000 °C, the porous LSCF exhibited rapid degradation accompanied by the severe SrZrO<sub>3</sub> formation. By contrast the dense LSCF only showed localized SrZrO<sub>3</sub> grains, which could be attributed to the air-tight

interface for dense LSCF which would minimize microstructural degradation near the oxygen/LSCF/GDC triple phase boundary [52].

De Vero et al. [58] also investigated the effect of single crystal GDC films on Sr and Zr transport of model LSCF/GDC/YSZ triplets, in which the single crystal GDC was epitaxially grown on the (100) and (111) single crystal YSZ substrates. The results showed that the single crystal GDC barrier layer could successfully prevent severe Sr diffusion into the YSZ electrolyte [58]. However, Zr could actively transport in the (100)-oriented GDC film, which was accompanied with severe pore formation and nanosized SrZrO<sub>3</sub> formation, whereas (111) GDC exhibited stronger ability to limit Zr diffusion.

Fig. 11 illustrates the comparison of Sr and Zr diffusion in different LSCF/GDC/YSZ triplets with polycrystalline, (100) and (111)-oriented GDC barrier layers [58]. Sr moves faster in polycrystalline GDC than that in single crystal GDC, because Sr can transport fast in the pathway of grain boundary diffusion. Zr has higher diffusivity in (100) than (111)-oriented GDC, which is due to the weak atomic bonds of GDC(100) attributed to less packing density than (111) [58], corresponding to the dislocation pipe diffusion mechanism for Zr.

Though not reported as commonly as in LSM-based SOEC, the delamination of LSCF can also be observed. Pan et al. [53] observed the LSCF anode delamination when the three-electrode cell operated under 1 A/cm<sup>2</sup> anodic current at 800 °C for 24 h. SrZrO<sub>3</sub> was found and the degradation mechanism was provided, as shown in Fig. 12. In Fig. 12(a) [53], a thin but dense layer of SrZrO<sub>3</sub> second phase forms at the electrode-electrolyte interface. Then, the improved electronic conductivity and catalysis activity of the SrZrO<sub>3</sub> layer by Co-diffusion leads to the generation of oxygen at the SrZrO<sub>3</sub>-YSZ interface during the electrolysis test. However, the oxygen molecules generated cannot efficiently diffuse away to the atmosphere, due to the low porosity of the SrZrO<sub>3</sub> layer. The accumulated oxygen gradually weakens the bonding between the SrZrO<sub>3</sub> layer and the YSZ electrolyte, finally the complete delamination.

Cr and Sulfur poisoning at LSCF electrodes of SOEC is also of significance in terms of the long-term property. Wei et al. [60] found the deposition of SrCrO<sub>4</sub>, CrO<sub>2.5</sub> and Cr<sub>2</sub>O<sub>3</sub> phases on the surface of LSCF oxygen electrodes and their formation was closely related to the increased segregation of the SrO species under anodic polarization conditions. Sr segregation led to Sr deficiency at the A-site, thus deteriorating the electrocatalytic activity of the LSCF oxygen electrodes for OER. Kushi [61] studied the durability of a single SOEC at 0.3 A/cm<sup>2</sup> and 700 °C under different air supply conditions, and it was concluded that Sulfur poisoning of LSC air electrode was the primary reason for the high degree of degradation, which was accelerated by the high  $p_{O_2}$  at anode/electrolyte interface.

### 2.1.3. Degradation of newly developed oxygen electrodes

In hopes of improving the electrocatalytic performance or the stability of oxygen electrodes, new anode materials have been investigated. Kim-Lohsoontorn et al. [62] compared the electrochemical performance of SOECs based on composite LSM/YSZ and Ba<sub>0.5</sub>Sr<sub>0.5</sub>Co<sub>0.8</sub>Fe<sub>0.2</sub>O<sub>3-δ</sub> (BSCF) oxygen electrodes, and found that cells having BSCF oxygen electrodes showed greater performance than LSM/YSZ-based cells over the range of temperature. In the durability test under 0.3 A/cm<sup>2</sup>, 850 °C and 70% steam concentration, the BSCF cell showed a significant decay, while LSM/YSZ cell exhibited no discernible performance degradation. The authors associated the degradation of BSCF with the detachment of BSCF from the electrolyte.

More recently, nickelates with chemical formula Ln<sub>2</sub>NiO<sub>4+δ</sub> (Ln: La, Nd, Pr) have received much attention. These compounds belong to the first-order Ruddlesden-Popper series material A<sub>n+1</sub>B<sub>n</sub>O<sub>3n+1</sub> with  $n = 1$ , whose structure is an alternating array of one La<sub>2</sub>O<sub>2</sub> rock salt layer and one LaNiO<sub>3</sub> perovskite layer along the C-axis [63–73].



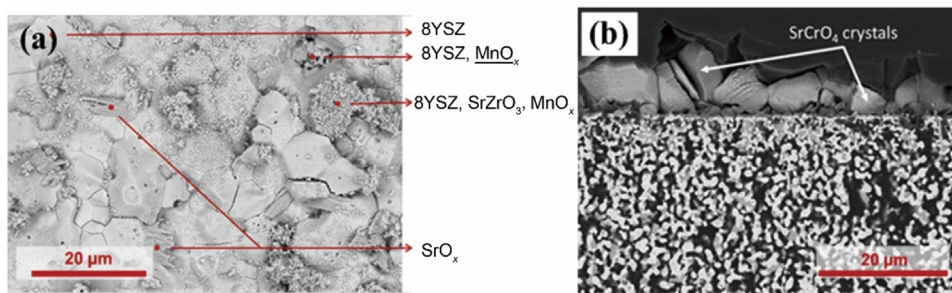


**Fig. 8.** [55] (a) SEM micrograph top view of the air electrode. (b) Cross-sectional SEM micrograph of air electrode near "air out". Large particles of  $\text{SrCrO}_4$  were formed on top of the air electrode and needles of  $\text{SrCrO}_4$  in the air electrode. Reproduced with permission from ref [58] under the license of Creative Commons. Copyright 2018.

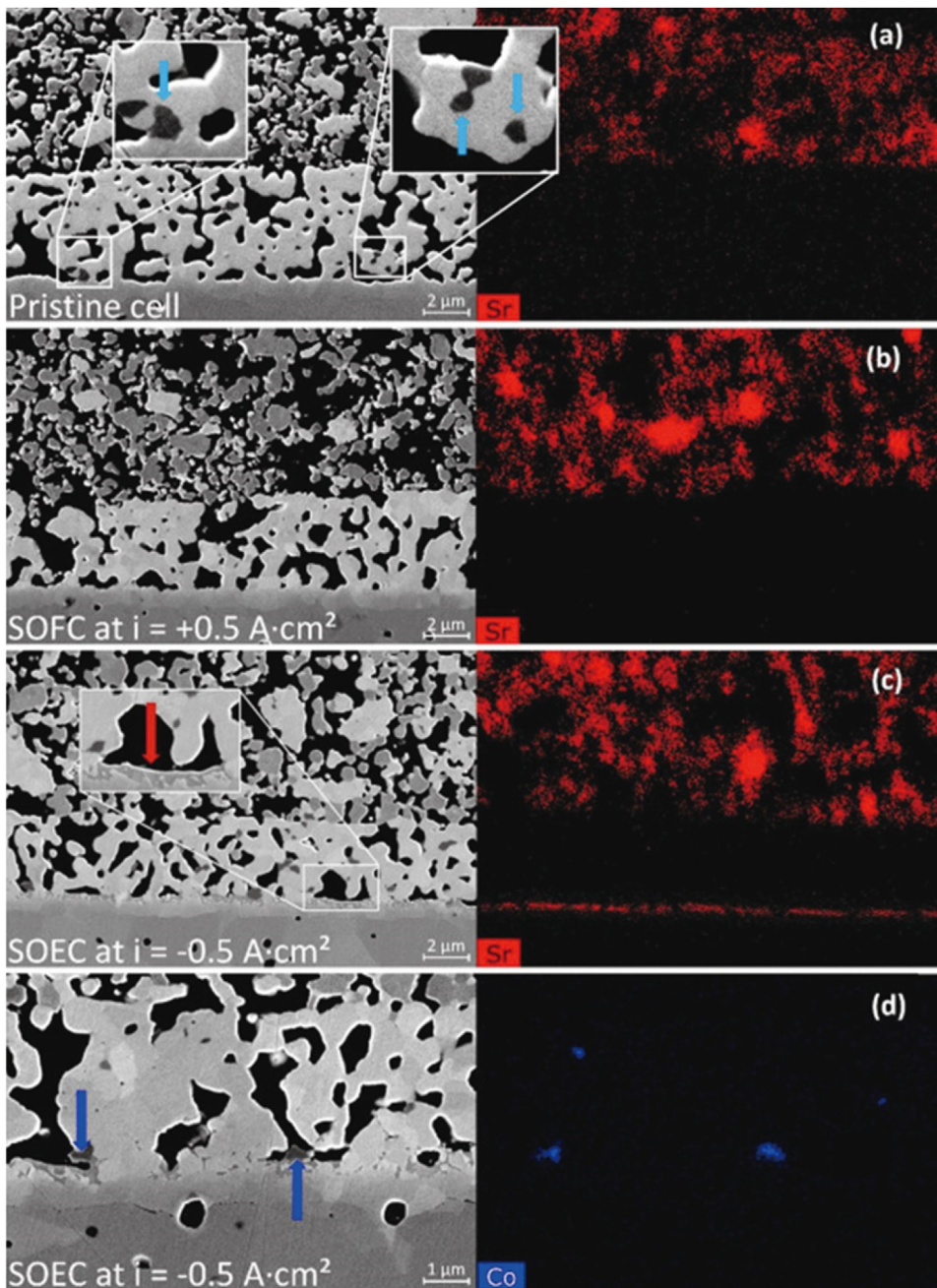


**Fig. 9.** [24] SEM-EDX images taken at YSZ-GDC interface (a) for the pristine cell, (b) for Cell operated in SOFC mode and (c, d) for Cell operated in SOEC mode. In (a), the Co-rich particles embedded in the bulk of the GDC network are highlighted by light blue arrows. In (c, d), the Sr-rich and Co-rich phases are highlighted on the SEM image with red and blue arrows respectively. Reproduced with permission from ref [24]. Copyright 2017 Elsevier, Inc.



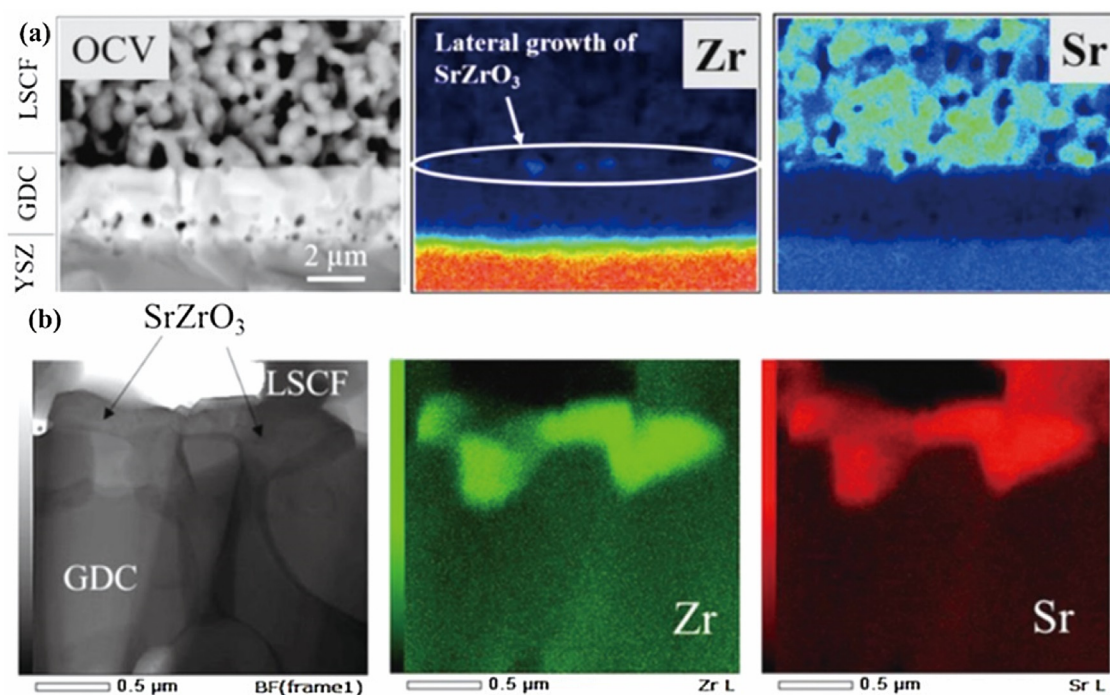


**Fig. 10.** [59] SEM-EDS cross-sectional mapping of LSCF/GDC/YSZ (a) under OCV, (b) STEM-EDS mapping of the LSCF/GDC interface after OCV showing the formation of SrZrO<sub>3</sub> at the O<sub>2</sub>/LSCF/GDC triple-phase boundary and extensively along the LSCF/GDC interface. Reprinted with permission from *J. Electrochem. Soc.*, 164, F259 (2017). Copyright 2017, The Electrochemical Society.

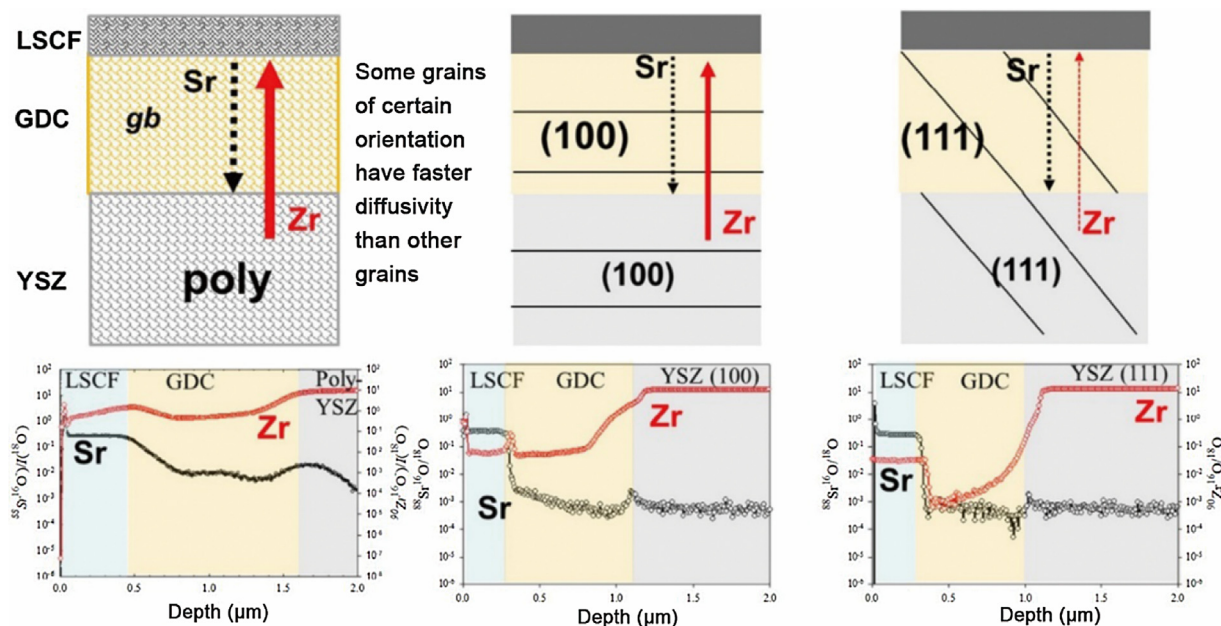


**Fig. 11.** [58] Schematic representation of the Sr and Zr diffusion in LSCF/GDC/YSZ triplets with GDC polycrystalline barrier layer, (100) and (111)-oriented epitaxial GDC barrier layers. Sr moves faster in polycrystalline GDC than that in single crystal GDC, because Sr can transport fast by grain boundary diffusion. Zr moves faster in (100) than (111)-oriented GDC, due to the weak atomic bonds of GDC(100) attributed to less packing density than (111). Reproduced with permission from ref [59]. Copyright 2018 Elsevier, Inc.

This structure can accommodate a large over-stoichiometry of oxygen, and the interstitial oxygen transport mechanism is believed able to mitigate the high oxygen pressure in the anode/electrolyte interface. Ogier et al. [74] investigated the electrochemical properties of Ln<sub>2</sub>NiO<sub>4+δ</sub> (Ln: La, Nd, Pr) on three electrode symmetrical half-cells under OCV and electrolysis conditions. The electrochemical characteristics were compared with those of the usual LSCF electrode. Under anodic polarization, in the temperature range

from 600 °C to 800 °C, the Pr<sub>2</sub>NiO<sub>4+δ</sub>-based cells exhibited the best performance, even more than 10 times higher than that of LSCF in a certain condition. However, Flura et al. [68] studied the chemical and structural changes in Ln<sub>2</sub>NiO<sub>4+δ</sub> (Ln: La, Nd, Pr) as a function of *p*<sub>O<sub>2</sub></sub> at high temperature. It was found Nd<sub>2</sub>NiO<sub>4+δ</sub> started to decompose into Nd<sub>2</sub>O<sub>3</sub> and NiO above 1000 °C, at *p*<sub>O<sub>2</sub></sub> = 10<sup>−4</sup> atm. Montenegro-Hernandez et al. [66] observed that Pr<sub>2</sub>NiO<sub>4+δ</sub> decomposed after 24 h of annealing at 700 °C and 900 °C.

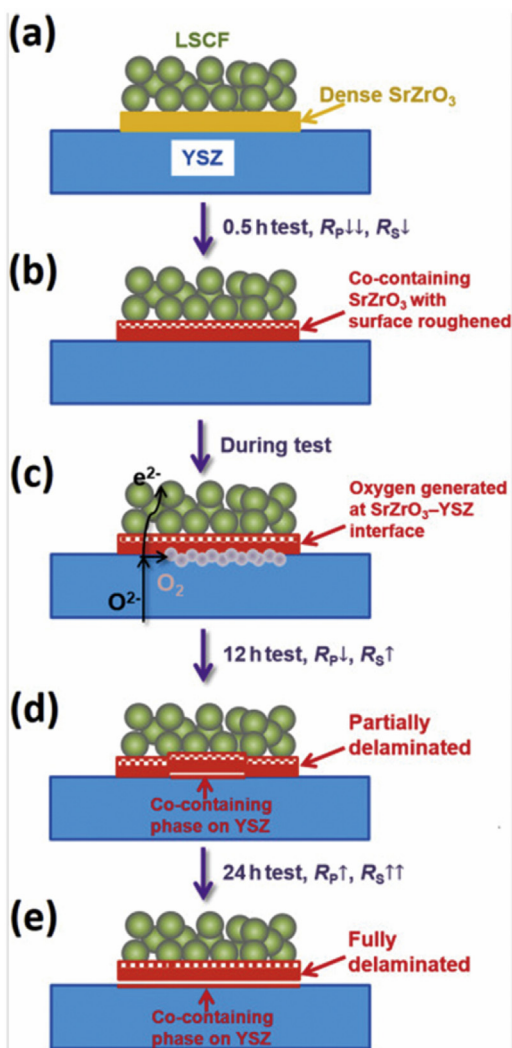


**Fig. 12.** [53] Schematic of the mechanism for the activation and delamination of LSCF air electrode (a) Freshly prepared sample; (b) Sample after 0.5 h high-current electrolysis; (c) Sample during the high-current electrolysis test; (d) Sample after 12 h electrolysis test; (e) Sample after 24 h electrolysis test. Reproduced with permission from ref [56]. Copyright 2018 Elsevier, Inc.

Double perovskite materials such as  $\text{Sr}_2\text{Fe}_{1.5}\text{Mo}_{0.5}\text{O}_{6-\delta}$  (SFM) and  $\text{GdBaCo}_2\text{O}_{5+\delta}$  were also studied as oxygen electrodes in SOEC. Wang et al. [75] studied the performance of co-electrolysis with SFM/SDC electrodes on a symmetrical cell. The co-electrolysis cells showed the good performance of  $0.734 \text{ A/cm}^2$  at  $850^\circ\text{C}$  under  $1.3 \text{ V}$ . However a degradation rate of  $10\%/kh$  was observed under the constant current density of  $0.12 \text{ A/cm}^2$  at  $800^\circ\text{C}$ . Wer et al. [76] investigated the electrochemical activity and microstructure evolution of layered  $\text{GdBaCo}_2\text{O}_{5+\delta}$  oxygen electrode under SOEC operation conditions at  $750^\circ\text{C}$  in air. The results demonstrated that anodic polarization resulted in obvious performance loss because of the deactivation of electrode activity, which could be mainly ascribed to the formation of BaO-like surface insulating phase. Higher anodic current density led to a more significant decrease of electrode performance due to the formation of more pronounced precipitation on the electrode surface, as seen in Fig. 13.

## 2.2. Electrolyte degradation

Candidates of electrolyte materials of SOEC are typically zirconia-based, ceria-based and  $\text{LaGaO}_3$ -based oxides [77]. Cerium oxide is often doped with  $\text{Gd}_2\text{O}_3$  (GDC) or  $\text{Sm}_2\text{O}_3$  (SDC), which

shows excellent oxygen conductivity, much higher than YSZ. However, because of the partial reduction of  $\text{Ce}^{4+}$  to  $\text{Ce}^{3+}$  in the cathode, only a few works have been focused on GDC under electrolysis. Eguchi et al. [78] studied cells operated in both SOFC and SOEC modes using zirconia-based and ceria-based electrolyte. It was found that the high applied voltage inevitably caused the reduction of  $\text{Ce}^{4+}$  to  $\text{Ce}^{3+}$  and deterioration of ionic transference number. It was concluded that because the unsteady electrolysis of ceria proceeded from the cathode side, the bare ceria electrolyte cannot be applied as the electrolyte for SOEC.

Doped lanthanum gallate, such as doped with strontium on the lanthanum site and magnesium on the gallium site (LSGM), is another candidate for SOEC electrolyte materials. It is also an excellent oxygen ion conductor over a broad range of temperatures, exhibiting an ionic transference number close to unity [79]. However, the incompatibility of nickel-based hydrogen cathode and LSGM electrolyte is a problem because of the formation of  $\text{LaNiO}_3$  [80–82] and fractures due to the thermal expansion coefficient (TEC) mismatch between electrolyte and electrodes [83].

Doped zirconia, especially YSZ, is the most commonly used electrolyte so far, as it has great chemical stability in both very reducing and oxidizing atmosphere and great ionic conductivity in high-temperature. However, YSZ still suffers the degradation in the high corrosive environment of electrolysis. Tietz et al. [51] investigated the long-term stability of a circular Ni/YSZ supported SOEC with an active cell area of  $45 \text{ cm}^2$ , which consisted of a YSZ electrolyte, a GDC barrier layer and a LSCF cathode. The cell operated under  $1 \text{ A/cm}^2$  electrolytic current load and  $780^\circ\text{C}$  for 9000 h, showing an average degradation rate of  $3.8\%/kh$ . Fig. 14(a) shows a pronounced grain structure of the electrolyte indicating a fracture mode along grain boundaries. The horizontally aligned pores throughout the electrolyte are also clearly observed indicated by arrows in Fig. 13(b) and (c). Fig. 14(d) shows the differently oriented grain surfaces exposed to varying, angle-dependent potential strength which is visible as a surface-dependent void structure on the grain surfaces.

Knibbe et al. [28] observed the intergranular fracture and pore formation along the grain boundaries of YSZ electrolyte near the anode/electrolyte interface after steam electrolysis at  $1\text{--}2 \text{ A/cm}^2$ . As shown in Fig. 15(a), a high density of  $30 \text{ nm}$  sized porelike holes or pores that were light in the image could be seen along the YSZ grain boundaries near the interface [28]. Such a high density of pores would decrease the contact between YSZ grains and then cause the increase of ohmic resistance, leading to degradation. Fig. 15(b) is the elements distribution across two YSZ grains showing a slight increase of oxygen in the porous region.

Laguna-Bercero et al. [84] investigated the electrolyte degradation in cathode-supported microtubular YSZ-based SOEC at high voltages up to  $2.8 \text{ V}$ . It was found that the cell voltage tended to saturate at high steam conversion rates, which was attributed to the electro-reduction of the thin YSZ electrolyte which induced electronic conduction losses. Severe electrolyte reduction of operated cells induced irreversible damage at the YSZ by the formation of voids at the grain boundaries of the dense YSZ electrolyte.

Jiang et al. [26] also observed the significant structural damage to the YSZ electrolyte particularly in the case of thick YSZ electrolyte cells. It was found that holes in the size of  $\sim 200 \mu\text{m}$  were formed in the delaminated LSM electrode and cavities of similar size on the YSZ electrolyte surface. In the center of the cavity, the morphology was characterized by grain and grain boundaries, while the region away from the cavity was similar to that of the fractured surface of YSZ. The significant microstructure differences between the center of the cavity and its surrounding regions disclose that the central area of the cavity was originally the closed internal pores in the YSZ electrolyte, while the fractured areas are the results of the forced



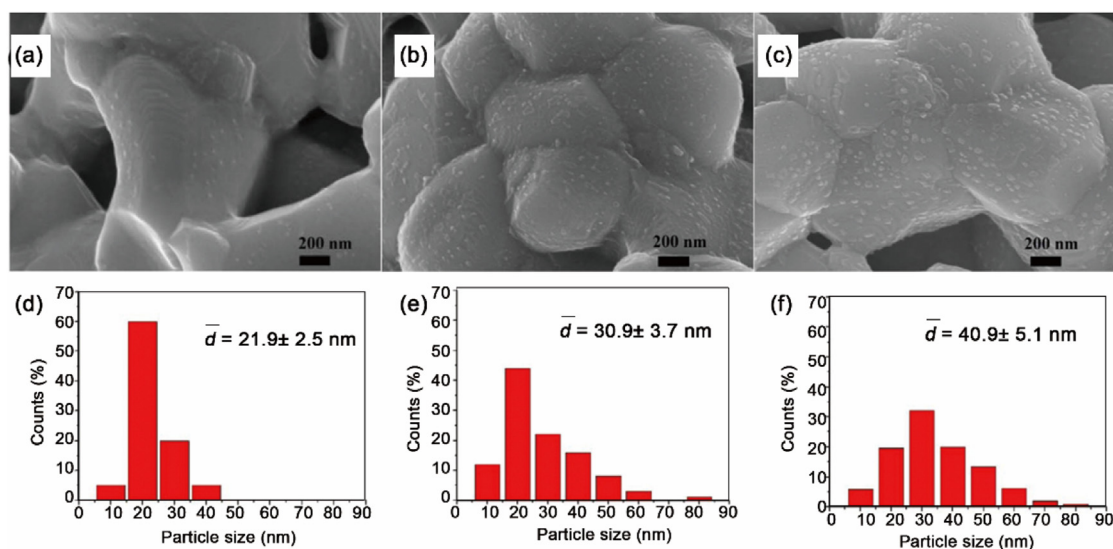


**Fig. 13.** [76] SEM images of (a) fresh GBCO, (b) after polarization at 300 mA/cm<sup>2</sup>, and (c) 600 mA/cm<sup>2</sup>. (d)–(f) The corresponding particle size distribution of surface precipitates for SEM images of (a)–(c). Reproduced with permission from ref [77]. Copyright 2018 Elsevier, Inc.

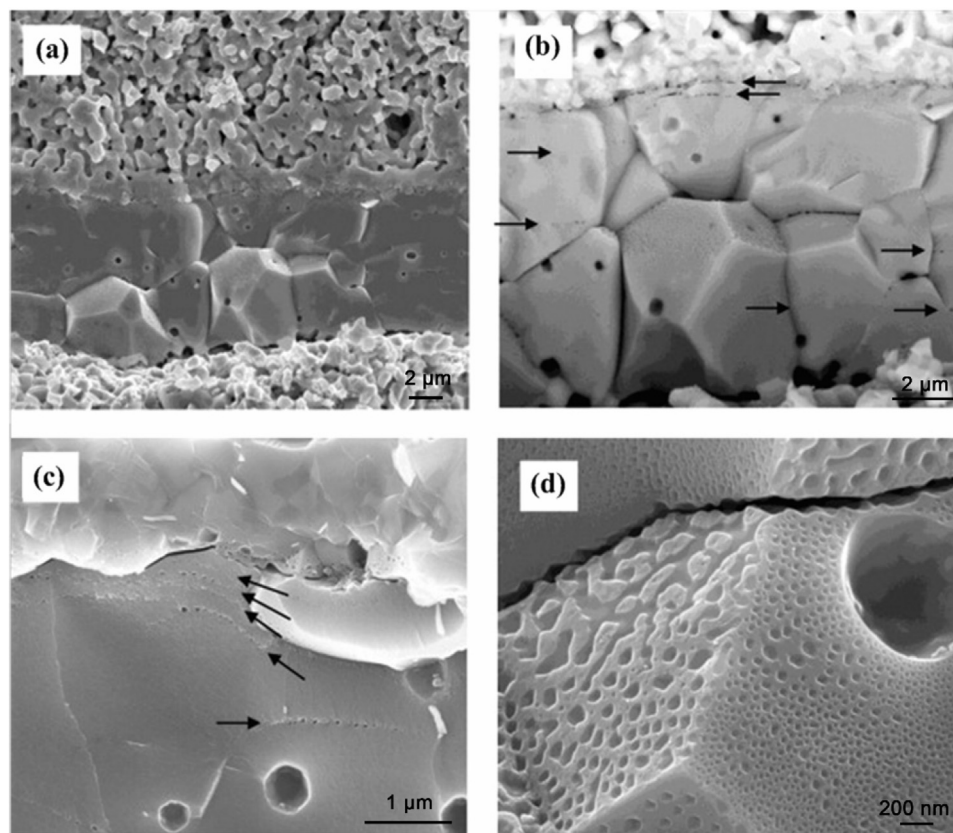


**Fig. 14.** [51] Images of fracture surfaces of the electrolyte layer. (a) Area of inter- and intragranular fracture, (b) same region in back-scattering mode showing more clearly horizontally structured pores (arrows) over the entire electrolyte layer and (c) at the GDC/YSZ interface, (d) highly enlarged YSZ grain surface with fractured grain boundary. Reproduced with permission from ref [54]. Copyright 2013 Elsevier, Inc.

separation of the electrolyte by the high  $p_{O_2}$  built-up within the closed pores of YSZ during electrolysis.

### 2.3. Hydrogen/cathode degradation

The most widely applied cathode for SOEC is Ni-based electrode, such as Ni-YSZ composite cathode. Nickel accommodates electrons transport, and YSZ provides paths for oxygen ions diffusion and

serves as an inhibitor for the coarsening of nickel particles during operation. This material exhibits high electronic conductivity and an excellent catalytic and electrochemical catalytic capability [27].

However, Ni-based cathode suffers nickel relocation. The et al. [49] investigated the microstructural evolution of SOEC by comparing long-term operation cells (6100 h and 9000 h) with a non-operated one. A homogeneous distribution of elements O, Ni, Y and Zr was observed for the non-operated cell, as shown



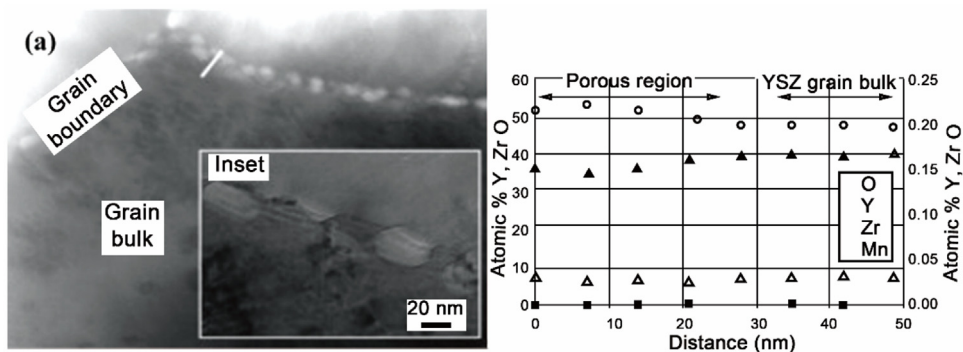


**Fig. 15.** [28] (a) TEM micrograph of YSZ grain boundary near the oxygen electrode. Inset: Higher magnification image of the grain boundary. (b) EDXS across the grain boundary as marked in (a). Reprinted with permission from *J. Electrochem. Soc.*, 157, B1209 (2010). Copyright 2010, The Electrochemical Society.

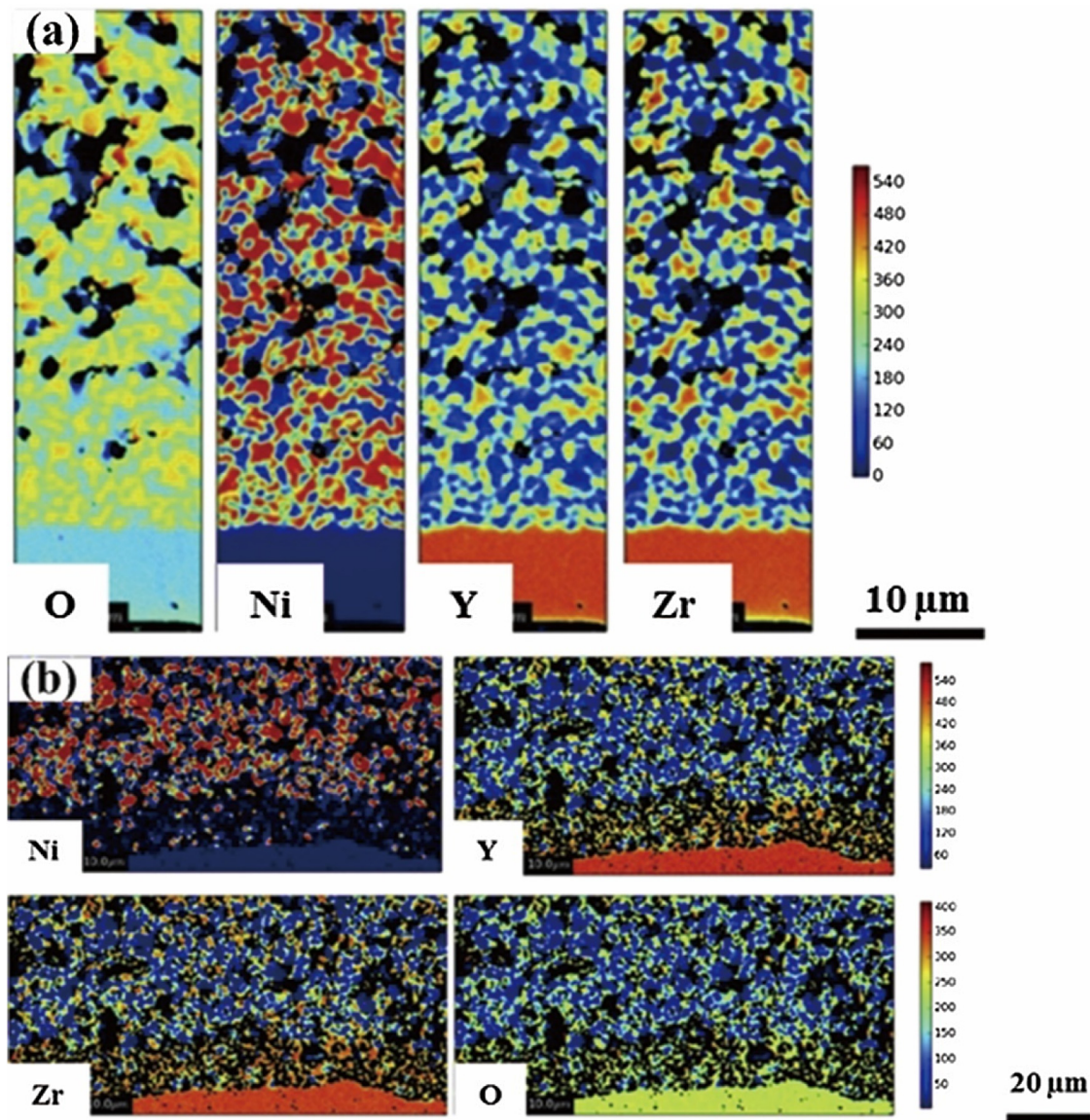


**Fig. 16.** [49] Electron probe micro analysis (EPMA) results of O, Ni, Y and Zr in the dense electrolyte YSZ (lower part) and the porous cathode (upper part) of (a) a non-operated cell and (b) an operated electrolysis cell under 1 A/cm<sup>2</sup> and 775–782 ° for 9000 h. Reproduced with permission from ref [52]. Copyright 2015 Elsevier, Inc.

in Fig. 16(a). In contrast, a significant agglomeration and depletion of nickel were found at the cathode/electrolyte interface for the 9000 h operated cell at 1 A/cm<sup>2</sup>, 780 °C and 80% absolute feed humidity, as seen in Fig. 16(b): nearly no nickel was

left in the first 10 μm away from the cathode/electrolyte interface and nickel agglomerated in the upper part. The depletion of Ni at the interface severely reduced the density of triple phase boundary of the cathode side, decreased the electronic conduc-

tion and increased the thickness of electrolyte, thus leading to large performance degradation. Ni relocation was also responsible for the formation of a 2–4  $\mu\text{m}$  thick dense layer of Ni/YSZ, formed at the cathode/electrolyte interface of a cell operated under 2 A/cm<sup>2</sup>, 90% humidity and 950 °C, as reported by Hauch et al. [85]. Other works concerning the influence of steam concentration on the Ni-based electrode can be referred to refs [86–90]. Indeed, water can react with nickel in the cathode to form various volatiles species, such as Ni(OH)<sub>2</sub>. These species diffuse and are further deposited on the surface of YSZ [27]. Humidity gradient driving vaporization–deposition mechanism causes the growth and merging of independent nickel droplets [87].

The Ni-based cathode can be damaged by impurities such as silicon from glass sealant or from raw materials. Hauch et al. [85,91] studied the silicon segregation in the Ni/YSZ electrode by conducting cell testing at a variety of operation temperatures, current densities and gas flows for over than 1000 h. Results showed a significant accumulation of SiO<sub>2</sub> in the few micrometers of the Ni-YSZ electrode close to the YSZ electrolyte [91]. In the cell operated under 0.5 A/cm<sup>2</sup>, 90% steam and 850 °C electrolysis for 1000 h, it was proven by EDX that the Si-containing impurities clearly segregated to the three-phase boundary (3PB) at the electrode/electrolyte interface and as grains of impurities with diameter up to 1  $\mu\text{m}$  [91], while in the test of 1 A/cm<sup>2</sup>, 70% steam and 850 °C electrolysis for 1600 h, impurities tended to segregate to the two-phase boundary (2PB) between the Ni and the YSZ where thin (40–70 nm) Si-containing rims formed [91].

A proposed mechanism of silicon deposition is introduced [6,92]: (1) in highly humidified atmospheres, Si evaporates from the glass seal in the form of Si(OH)<sub>4</sub>(g), which deposits at the TPB and is transformed into SiO<sub>2</sub>(s); (2) under high cathodic polarization, Si may dissolve into Ni particles at the TPB further because the solubility limit of Si in Ni is 14 mol% at 850 °C; (3) when the oxidation of the atmosphere is strong enough, the dissolved Si can be re-oxidized into SiO<sub>2</sub>(s) at a later stage.

Additionally, impurities in the inlet gases stream, most likely sulfur are reported to influence the stability of Ni/YSZ electrode [93–96]. Ebbesen et al. [96] examined the initial performance and electrolysis durability of Ni/YSZ cathode supported cells by applying either industrial grade gases with minute impurities or cleaned gases. Steam, CO<sub>2</sub> and co-electrolysis stability tests were conducted in both gas atmospheres in 850 °C for over 600 h. It was found that, for all electrolysis tests, the cells substantially degraded when applying gases with impurities, however the application of clean gases to the Ni/YSZ electrode resulted in operation without degradation, even some cells showed slight activation [96]. EIS results showed that the poisoning effect was related to the adsorption of impurities at the TPB [96]. It was disclosed that physical absorption of sulfur blocked the reaction sites and chemical reaction of sulfur forms nickel sulfide [93].

In the case of CO<sub>2</sub> electrolysis or co-electrolysis, the oxidation of Ni to NiO and coking are the potential issues to Ni-based cathode [1,26,97]. Wang et al. [98] examined a pure Ni cathode and various Ni-based bimetallic cathodes in LSGM electrolyte-supported cells for CO<sub>2</sub> electrolysis at a temperature from 700 °C to 900 °C. In the case of the pure Ni cathode, despite of the high activity in the initial performance, coke formation was observed after test in the atmosphere of 50% CO<sub>2</sub>, 1% CO and 49% Ar. Fig. 17(a)–(c) show the microstructures of pure Ni and NiFe91 (weight ratio Ni/Fe = 9:1) cathodes after CO<sub>2</sub> electrolysis operation at 800 °C. The micrograph of pure Ni cathode reveals the presence of small needle-like structure, which is probably the deposited carbon. However, no such clear coking could be seen in the image of NiFe91 cathode. Fig. 17(d) is the Raman spectra of the cathode surface of pure Ni and NiFe91 after CO<sub>2</sub> electrolysis tests, which proves the coking of pure Ni cathode and indicates the capability of Fe

of preventing the coke formation. Concerning this disadvantages of Ni-based cathode associated with coking, many cement cathodes were proposed, such as Ni-Fe-La(Sr)Fe(Mn)O<sub>3</sub> [97], oxygen deficient perovskite La<sub>0.6</sub>Sr<sub>0.4</sub>Fe<sub>0.8</sub>Ni<sub>0.2</sub>O<sub>3- $\delta$</sub>  cathode with in-situ exsolved Fe-Ni bimetallic nanospheres [99] and vanadium-doped LaFeO<sub>3</sub> (LSFV<sub>x</sub>) cathode [100].

### 3. Status of electrode/electrolyte interfaces governed by $p_{\text{O}_2}$

Although having similar or identical components with SOFC, SOEC usually suffers greater degradation rate [84]. It is natural to examine the differences between SOEC and SOFC to locate the reason for the higher degradation of SOEC. From the viewpoint of electrochemistry, SOEC differs from SOFC in the distribution of  $p_{\text{O}_2}$  or the chemical potential of oxygen ( $\mu_{\text{O}_2}$ ) across the whole cell, especially at the electrode/electrolyte interfaces.

For oxygen conducting SOEC, the reaction of interest is as follows:



In equilibrium, it leads to

$$\frac{1}{2}\mu_{\text{O}_2} + 2\tilde{\mu}_{\text{e}} = \tilde{\mu}_{\text{O}^{2-}} \quad (8)$$

where,  $\tilde{\mu}_{\text{O}^{2-}}$  is the electrochemical potential of oxygen ions, and  $\tilde{\mu}_{\text{e}}$  is the electrochemical potential of electrons.

$p_{\text{O}_2}$  is related to  $\mu_{\text{O}_2}$  by

$$\mu_{\text{O}_2} = \mu_{\text{O}_2}^0 + RT \ln p_{\text{O}_2} \quad (9)$$

Note that  $p_{\text{O}_2}$  and  $\mu_{\text{O}_2}$  are practically the same concepts, both will be used alternately in the following discussion.

Therefore, if we place an oxygen conductor in an atmosphere with a specific  $p_{\text{O}_2}$  and the equilibrium Eq. (7) is achieved, the  $p_{\text{O}_2}$  represent the values of  $\tilde{\mu}_{\text{O}^{2-}}$  and  $\tilde{\mu}_{\text{e}}$ . Because  $\tilde{\mu}_{\text{O}^{2-}}$  and  $\tilde{\mu}_{\text{e}}$  represent the degree of oxygen non-stoichiometry, the  $p_{\text{O}_2}$  in the atmosphere is related to oxygen non-stoichiometry of the material. Then it is applicable and convenient to apply the  $p_{\text{O}_2}$  in the atmosphere to describe the status of the material. This is how the concept of  $p_{\text{O}_2}$  of a material is established.

However, if we would like to apply the concept of  $p_{\text{O}_2}$  within a material which is under a condition with different  $p_{\text{O}_2}$ , such as SOEC or oxygen permeation membrane, the concept of local equilibrium [101] would be introduced in. As suggested by Virkar [102–109], the important implication of local equilibrium in this case is that the equilibrium Eq. 7 is valid everywhere in the system. This means if a pore of volume  $V_{\text{pore}}$  exists at some position in the conductor, the  $p_{\text{O}_2}$  in the pore would correspond to the local  $\mu_{\text{O}_2}$ . If the pore volume approaches to zero, the number of moles of oxygen in the pore,  $n_{\text{O}_2}$ , approaches zero as well, assuming the ideal gas law. Therefore, though no actual pore exists, the concept of  $p_{\text{O}_2}$  and  $\mu_{\text{O}_2}$  however continue to exist. This is how the concept of  $p_{\text{O}_2}$  is well defined within an oxygen conductor by Virkar, which is illustrated in Fig. 18 [102].

After the establishment of the concept of local  $p_{\text{O}_2}$ , the distribution of  $p_{\text{O}_2}$  within a material can be accessed to. Virkar et al. have conducted extensively research on the determination of  $p_{\text{O}_2}$  within a solid oxide cell electrolyte or a MIEC membrane theoretically [102,103,106–109] and experimentally [104,105]. In addition to local equilibrium, the transport theory that the transport of a charged species occurs down its electrochemical potential gradient is needed [105]. Therefore, the current density due to oxygen ions and electrons are given by:

$$I_{\text{e}} = -\frac{\sigma_{\text{e}}}{(-1)\text{e}} \nabla \tilde{\mu}_{\text{e}} = \frac{\sigma_{\text{e}}}{\text{e}} \frac{d\tilde{\mu}_{\text{e}}}{dx} \quad (10)$$



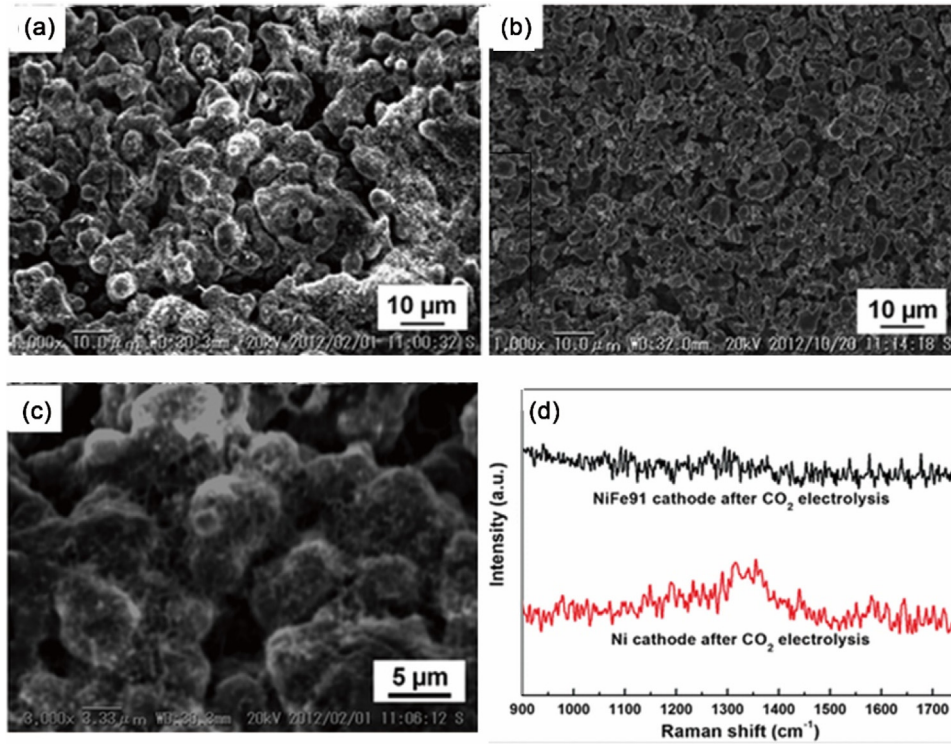


**Fig. 17.** [98] Morphology of (a and b) Ni cathode (c) NiFe91 (weight ratio 9:1) cathode for the cells after CO<sub>2</sub> electrolysis operation at 800 °C. (d) Raman spectra of the surface of Ni and NiFe91 cathodes. Reproduced with permission from ref [99]. Copyright 2013 Royal Society of Chemistry.

$$I_i = I_{O_2^-} = -\frac{\sigma_{O_2^-}}{(-2)e} \nabla \tilde{\mu}_{O_2^-} = \frac{\sigma_i}{2e} \frac{d\tilde{\mu}_{O_2^-}}{dx} \quad (11)$$

where,  $I_e$  is the electronic current density;  $\sigma_e$  is the electronic conductivity of the material.  $I_i$  ( $I_{O_2^-}$ ) is the ionic (oxygen) current density;  $\sigma_i$  ( $\sigma_{O_2^-}$ ) is the ionic (oxygen) conductivity of the material.

Considering the local equilibrium, the current density of oxygen ions can be represented in terms of  $\mu_{O_2}$  and  $\tilde{\mu}_e$ :

$$I_i = \frac{\sigma_i}{2e} \frac{d}{dx} (\tilde{\mu}_{O_2^-}) = \frac{\sigma_i}{2e} \frac{d}{dx} \left( \frac{1}{2} \mu_{O_2} + 2\tilde{\mu}_e \right) = \frac{\sigma_i}{4e} \frac{d\mu_{O_2}}{dx} + \frac{\sigma_i}{e} \frac{d\tilde{\mu}_e}{dx} \quad (12)$$

Eqs. (10)–(12) are valid not only for typical MIECs, but also for predominantly ionic conductors such as YSZ. However, it is worth noting that, for predominantly ionic conductors, the electronic current cannot be neglected, no matter how small the electronic current is. This is because the assumptions of local equilibrium and the simultaneous neglect of electronic conduction are contradictory assumptions [102].

Therefore, from the transport of oxygen ions across interface I in Fig. 18 [102]:

$$\mu'_{O_2} = \mu_{O_2}^I + 4e(r'_i I_i - r'_e I_e) \quad (13)$$

From the transport of oxygen ions across interface II:

$$\mu''_{O_2} = \mu_{O_2}^{II} - 4e(r''_i I_i - r''_e I_e) \quad (14)$$

where,  $\mu'_{O_2}$  is the  $\mu_{O_2}$  within the membrane, just inside electrode I/membrane interface;  $\mu''_{O_2}$  is the  $\mu_{O_2}$  within the membrane, just inside electrode II/membrane interface.  $r'_i$  and  $r''_i$  are the area specific ionic resistances of interface I and II, respectively, which are actually the ion charge transfer resistances.  $r'_e$  and  $r''_e$  are the area specific electronic resistances for direct electron transfer across the

interface I. In the semiconductor terminology,  $r'_e$  and  $r''_e$  are area specific contact resistances (non-ohmic contact) [107].

And the generalized form of  $\mu_{O_2}$  as a function of position in a membrane without the incorporation of interfaces can be given by:

$$\mu_{O_2}(x) = \mu_{O_2}^I + 4e(I_i + I_e) \int_0^x \frac{dx}{\sigma_i(x)} + 4e \int_{\phi^I}^{\phi(x)} \left( \frac{\sigma_i(x) + \sigma_e(x)}{\sigma_i(x)} \right) d\phi(x) \quad (15)$$

Note that we use Eq. (15) only to indicate the continuum distribution of  $p_{O_2}$  in the membrane without incorporation of interfaces and the focus of discussion is still the electrode/membrane interfaces.

As evident from Eqs. (13) and (14), the values of  $\mu'_{O_2}$  and  $\mu''_{O_2}$  depend upon the values of  $r'_i$ ,  $r''_i$ ,  $r'_e$ ,  $r''_e$ ,  $I_i$  and  $I_e$ . If we apply the presented general discussion for SOFC and SOEC, the illustrative results can be shown in Fig. 19 [102]. For SOFC in a certain condition, the distribution of  $\mu_{O_2}$  in the electrolyte is within the two  $\mu_{O_2}$  limits in the two gas phases. However, for SOEC, the values of  $\mu'_{O_2}$  and  $\mu''_{O_2}$  can exceed the chemical potential of oxygen in the corresponding gas phase. This indicates that, in SOEC mode, the  $p_{O_2}$  in the electrolyte near the cathode/electrolyte interface is lower than the  $\mu_{O_2}$  in gas phase, suggesting the possibility of decomposition of electrolyte [102]. On the anode side, a high  $p_{O_2}$  can be established in the electrolyte just near the anode/electrolyte interface, resulting in the delamination of anode if the pressure is sufficient to cause local mechanical cracking [107].

Based on his developed theory, Virkar [107] performed an illustrative calculation of  $p_{O_2}$  ( $p_{O_2}^a$ ) at the anode/electrolyte interface (LSM/YSZ||YSZ). It was found that this value was substantially influenced by the electronic resistance of electrolyte:

$$p_{O_2}^a = p_{O_2}^{Ox} \exp \left( -\frac{4F}{RT} \left\{ \frac{E_A r_e^a}{R_e} - \frac{(E_A - E_N) r_i^a}{R_i} \right\} \right) \quad (16)$$

where,  $p_{O_2}^{Ox}$  is the oxygen partial pressure in the gas phase of the anode,  $E_A$  is the applied electrolysis voltage,  $E_N$  the Nernst potential,



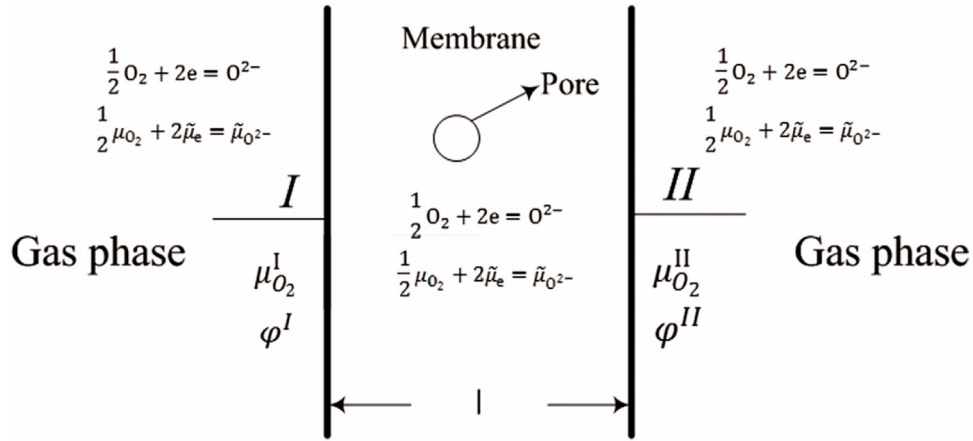


**Fig. 18.** [102] A schematic illustration of the definition of local  $p_{O_2}$  within a membrane of a MIEC. The thickness of the membrane is  $l$ .  $\mu_{O_2}^I$  is the  $\mu_{O_2}$  in the gas phase of electrode I;  $\mu_{O_2}^{II}$  is the  $\mu_{O_2}$  in the gas phase of electrode II.  $\phi^I$  and  $\phi^{II}$  are the reduced (negative) electrochemical potential of I and II, respectively. Local equilibrium in the system implied that  $\frac{1}{2}\mu_{O_2} + 2\mu_e = \mu_{O_2^{2-}}$  is valid everywhere. This means if a pore of volume  $V_{pore}$  exists at some position in the conductor, the  $p_{O_2}$  in the pore would correspond to the local  $\mu_{O_2}$ . If the pore volume approaches to zero, the number of moles of oxygen in the pore,  $n_{O_2}$ , approaches zero as well, assuming ideal gas law. Therefore, though no actual pore exists, the concept of  $p_{O_2}$  and  $\mu_{O_2}$  however continue to exist. Yet the local  $p_{O_2}$  is well defined. Reproduced with permission from ref [103]. Copyright 2005 Elsevier, Inc.

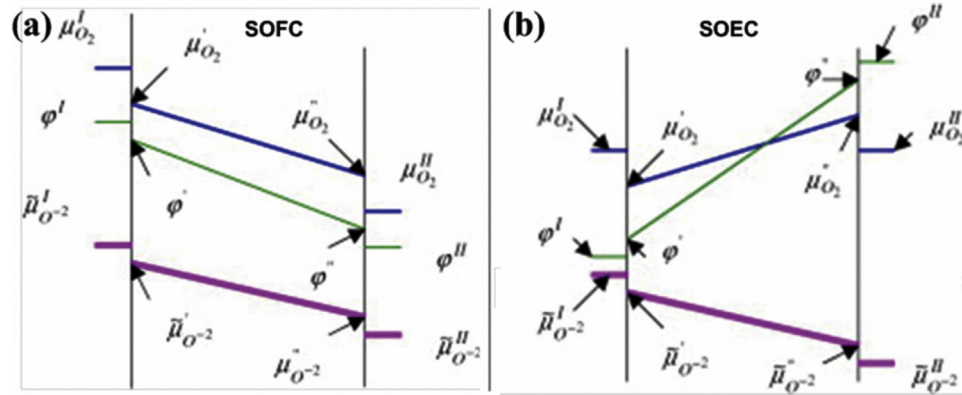


**Fig. 19.** [102] Schematic variations of  $\mu_{O_2}$ ,  $\mu_{O_2^{2-}}$  and  $\phi$  across the electrolyte and interfaces for (a) SOFC and (b) SOEC in certain conditions. Reproduced with permission from ref [103]. Copyright 2005 Elsevier, Inc.

**Table 1**

[107] Estimation of  $p_{O_2}$  within the electrolyte just near the oxygen electrode/electrolyte interface,  $p_{O_2}^a$ , for various values of cell area specific electronic resistance,  $R_e$ . The applied voltage is  $E_A = 1.5$  V.  $r_e^{el}$  is the electronic resistance of electrolyte.  $I_{total}$  is the total external current density. Reproduced with permission from ref [108]. Copyright 2010 Elsevier, Inc.

$r_e^{el}$ ( $\Omega$ cm <sup>2</sup> )	$R_e$ ( $\Omega$ cm <sup>2</sup> )	$R_i$ ( $\Omega$ cm <sup>2</sup> )	$I_i$ (A/cm <sup>2</sup> )	$I_e$ (A/cm <sup>2</sup> )	$I_{total}$ (A/cm <sup>2</sup> )	$p_{O_2}^a$ (atm)	Likelihood of delamination
0	1.5	0.39	1.117	1.0	2.117	$10^{-17}$	No delamination
1	2.5	0.39	1.117	0.6	1.717	$10^{-4}$	No delamination
5	6.5	0.39	1.117	0.23	1.347	1.44	No delamination
8	9.5	0.39	1.117	0.158	1.317	104.6	Delamination highly likely
20	21.5	0.39	1.117	0.07	1.187	$10^4$	Delamination imminent

$r_e^a$  is the area specific resistance for direct electron transfer across anode/electrolyte interface,  $r_i^a$  is the area specific resistance for ion charge transfer resistance at anode/electrolyte interface, which is effectively polarization resistance (excluding the porous electrode) and may be described using Butler-Volmer type of phenomenological models [107],  $R_i$  and  $R_e$  are the total ionic and electronic resistances of the whole SOEC, respectively.

In a typical cell with Ni/GDC cathode, it is suggested  $r_i^c \approx 0$  and  $r_e^c \approx 0$ . For the anode side,  $r_i^a \approx 0.3 \Omega$  cm<sup>2</sup> and  $r_e^a \approx 1.5 \Omega$  cm<sup>2</sup>. The ionic resistance of the electrolyte  $r_i^{el} \approx 0.09 \Omega$  cm<sup>2</sup>. By varying the electronic resistance of the electrolyte  $r_e^{el}$  from 0 to 20  $\Omega$  cm<sup>2</sup>, the  $p_{O_2}$  within the electrolyte just near the anode can be estimated.

At electrolysis voltage  $E_A = 1.5$  V, the results are shown in Table 1 [102].

The estimation results show that the electronic resistance of electrolyte can exert a significant impact on the value of the  $p_{O_2}$  within the electrolyte near the interface. Under a certain condition, the  $p_{O_2}$  can be as high as  $10^4$  atm, which would cause electrode delamination immediately. Therefore, the author suggested it be beneficial for the stability of SOEC to introduce some electronic conduction in the electrolyte.

Jacobsen and Mogensen [110] also examined the  $p_{O_2}$  across the electrolyte and at the electrode/electrolyte interfaces of SOEC, the distribution of which is shown in Fig. 20. The authors concluded that

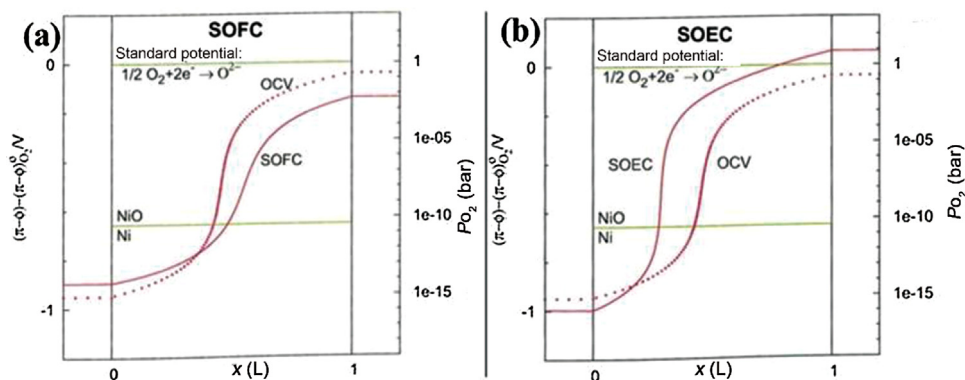


**Fig. 20.** [110]  $\pi - \phi$  (this is the electrode potential based on authors' definition) and equilibrium oxygen pressure in a cell operating in SOEC mode compared to OCV condition at 1000 °C. Reprinted with permission from ECS Transactions., 13, 259 (2008). Copyright 2008, The Electrochemical Society.

in steady state operation, the oxygen pressure inside a cavity within electrolyte near the interface cannot exceed the value corresponding to the electrode potential. However, when compared with the oxygen partial pressure near the anode/electrolyte interface under OCV, the  $p_{O_2}$  built under SOEC mode is higher. This means that cells working in SOEC mode may build up a detrimental interior  $p_{O_2}$  at the anode, causing delamination of the electrode or the electrolyte close to the anode.

The experimental measurement of  $p_{O_2}$  in the electrolyte film was conducted by Lim and Virkar [104,105], using platinum reference electrodes (probes) embedded within the electrolyte layer. It was found that the  $p_{O_2}$  dropped mainly across the cathode/electrolyte interface for an anode-supported fuel cell with GDC electrolyte [105]. Mineshige et al. [111] also measured the  $\mu_{O_2}$  variation in SDC electrolyte of a fuel cell by Raman spectroscopy. It was shown that most parts of SDC were mixed conductive because of the low  $\mu_{O_2}$  and only a thin layer adjacent to the air side remained dominantly ionic conductive under the OCP condition.

Atomic-scale simulation by density-functional-theory (DFT), first-principle theory and thermodynamic modeling was conducted to elucidate the mechanism of oxygen delamination of SOEC [112]. Fig. 21(a) shows the formation of peroxy O–O bonds (precursors of  $O_2$  molecules) at the (001) surface of cubic  $ZrO_2$  related to substitutional Mn impurities in the subsurface region. Fig. 21(b) illustrates the equilibrium pressure of the  $O_2$  gas above a free  $ZrO_2$  surface at  $T = 800^\circ C$  as a function of  $O_2$  formation energy corresponding to different subsurface substitutional defects. It was shown that La and Sr substitutional defects positioned in  $ZrO_2$  near LSM/YSZ interface significantly elevated oxygen formation energy, which may facilitate a high  $p_{O_2}$  build-up in the interfacial region and eventually develop delamination process. This mechanism, being different from what Virkar and Mogensen suggested, predicts that the high  $p_{O_2}$  would establish in the closed pores in the porous anode near the anode/electrolyte interface.

The presented principle investigations examined the  $p_{O_2}$  near the electrode/electrolyte interfaces, either within the electrolyte or in the closed pores in the electrode. Many numerical modeling works studied the  $p_{O_2}$  in the open pores in the electrode near the interface for solid oxide cells, by considering the gas transport theory and oxygen exchange reactions [113–118]. Laurencin et al. [24] investigated the degradation mechanism of LSCF/GDC composite electrode under SOEC mode by theoretical calculation and experiments. The modeling results showed that the  $p_{O_2}$  in the open pores in the electrode near the anode/electrolyte interface is only slightly higher than that in air.

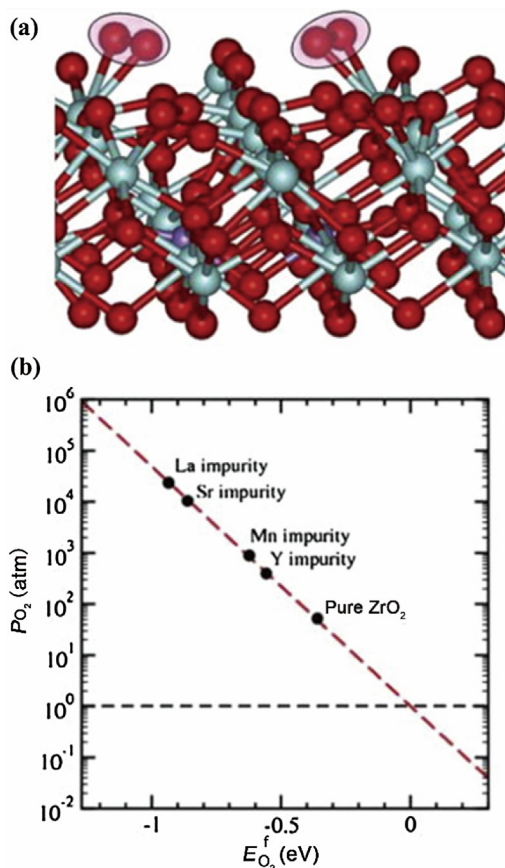


**Fig. 21.** [112] (a) Schematics of the formation of peroxy O–O bonds (precursors of  $O_2$  molecules) at the (001) surface of cubic  $ZrO_2$  related to substitutional Mn impurities in the subsurface region. Oxygen atoms are shown in red, Zr – as small light blue balls, Mn – in purple; (b) Equilibrium pressure of the  $O_2$  gas above a free  $ZrO_2$  surface at  $T = 800^\circ C$  as a function of  $O_2$  formation energy corresponding to different subsurface substitutional defects. (For interpretation of the references to color in this figure legend, the reader is referred to the web version of this article.) Reproduced with permission from ref [113]. Copyright 2012 Elsevier, Inc.

#### 4. Emerging mitigation strategies and proton-conducting SOEC

As discussed in the previous section, the degradation of SOEC anode is strongly related to the high  $p_{O_2}$  established near the anode/electrolyte interface, either within the electrolyte or in the

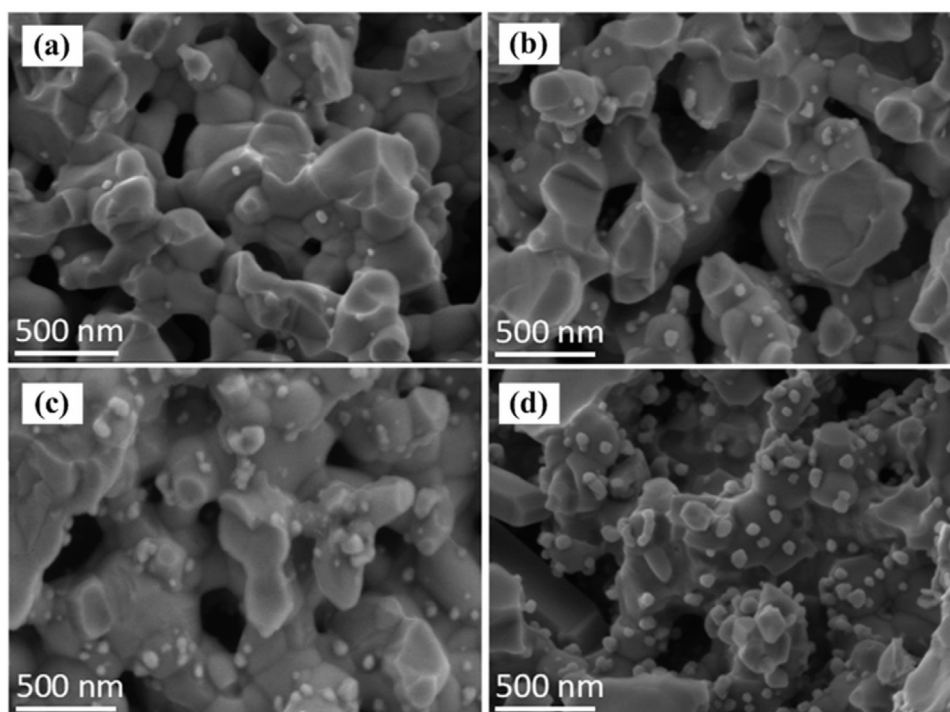


Fig. 22. [121] Morphologies of anode LSM/YSZ + (a) 2 wt%, (b) 4 wt%, (c) 6 wt% and (d) 8 wt%  $\text{RuO}_2$ . Reproduced with permission from ref [122]. Copyright 2018 Elsevier, Inc.

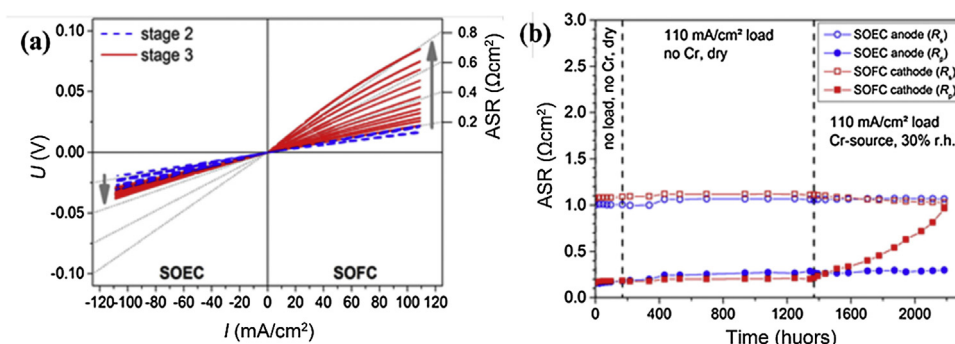


Fig. 23. [72] (a) The  $I$ - $V$  curves of the SOEC anode and SOFC cathode layers of the  $\text{La}_2\text{NiO}_{4+\delta} \parallel \text{GDC} \parallel \text{La}_2\text{NiO}_{4+\delta}$  symmetric cell at  $800^\circ\text{C}$  in air. (b) Degradation-induced changes in area specific resistance (ASR) of the SOEC anode and SOFC cathode sides, as determined by three-electrode impedance measurements at  $800^\circ\text{C}$ .  $R_s$  denotes the series resistance (mainly IR-drop across the electrolyte) while  $R_p$  refers to the polarization resistance of the electrodes. Reproduced with permission from ref [73]. Copyright 2017 Elsevier, Inc.

electrode closed pores. Thus, the key to improve the durability of SOEC anode is to reduce  $p_{\text{O}_2}$  near the interface. The principle behind the developed mitigation strategies is to lower the anodic overpotential: either reduce the activation overpotential or reduce the concentration polarization. The methods include infiltrating active nanoparticles, developing new materials and improving gas transport [26,119,120]. Here we would like to introduce some published works in the recent years to update the advances in anode mitigation strategies.

Infiltration has been found as an effective way to lower the activation overpotential and to improve the durability because of the extended reaction sites. Song et al. [121] studied the effectiveness of different weight percentages of  $\text{RuO}_2$  nanoparticles deposited on the surface of LSM/YSZ anodes by an infiltration method. The current density was improved from  $0.46 \text{ A/cm}^2$  to  $0.74 \text{ A/cm}^2$  at  $1.2 \text{ V}$  and  $800^\circ\text{C}$  after anchoring 6 wt.%  $\text{RuO}_2$  onto the surface of LSM/YSZ composite electrode, with the greatest enhancement of 60%. The morphologies of infiltrated anode are shown in Fig. 22. The durability test was conducted, showing negligible degradation

with constant current density  $0.4 \text{ A/cm}^2$  for over 240 min. Post-testing analysis found that  $\text{RuO}_2$  nanoparticles remained almost unchanged without agglomeration.

Zheng et al. [122] investigated the  $\text{La}_{0.8}\text{Sr}_{0.2}\text{Co}_{0.8}\text{Ni}_{0.2}\text{O}_{3-\delta}$  (LSCN) impregnated GDC/LSM composite oxygen electrode as a high-performance electrode for co-electrolysis. The LSCN impregnated cell exhibited the current density of  $1.60 \text{ A/cm}^2$  at  $1.5 \text{ V}$  at  $800^\circ\text{C}$  and showed stable performance without obvious degradation for more than 100 h. Shahrokhi et al. studied the electrochemical performance and stability of LSM oxygen electrodes infiltrated with  $\text{La}_2\text{Ni}_{0.5}\text{Co}_{0.5}\text{O}_4$  (Ruddlesden-Popper) and  $\text{LaNi}_{0.5}\text{Co}_{0.5}\text{O}_3$  (perovskite) nanoparticles under cyclic SOEC and SOFC modes. Results indicated that the addition of  $\text{La}_2\text{Ni}_{0.5}\text{Co}_{0.5}\text{O}_4$  nanoparticles had more impacts on polarization resistance reduction as compared to  $\text{LaNi}_{0.5}\text{Co}_{0.5}\text{O}_3$ , probably due to the facile oxygen transport in the rock salt layer of Ruddlesden-Popper structure. Analysis of the polarization resistance fluctuations showed better stability in Ruddlesden-Popper structure-infiltrated electrodes as compared to perovskite structure.



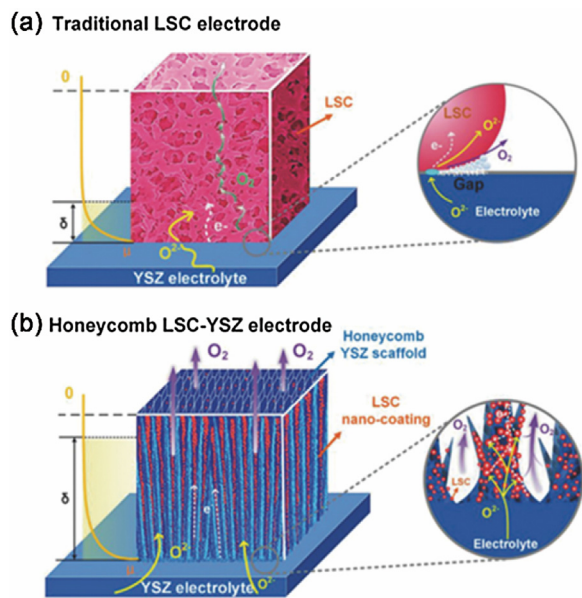


**Fig. 24.** [128] Schematic illustration of electrodes (a) traditional sponge-like LSC electrode (b) Honeycomb LSC/YSZ electrode. Reproduced with permission from ref [108]. Copyright 2018 John Wiley and Sons.

In addition to infiltration, another way to mitigate the high  $p_{O_2}$  is to use R-P phase materials, such as  $La_2NiO_{4+\delta}$ , as the oxygen electrode [123–125]. The attractive property of R-P phase materials is their aptitude to accommodate a large oxygen overstoichiometry, which is assumed to be able to mitigate the high  $p_{O_2}$  at the anode/electrolyte interface. Fig. 23(a) is the  $I$ - $V$  curves of the SOEC anode and SOFC cathode layers of the  $La_2NiO_{4+\delta} || GDC || La_2NiO_{4+\delta}$  symmetric cell at 800 °C in air [72]. It can be seen that the  $La_2NiO_{4+\delta}$  SOFC side suffers much more in resistance increase with time than the  $La_2NiO_{4+\delta}$  SOEC side, which indicates that  $La_2NiO_{4+\delta}$  is more stable and behaves much better under anodic polarization than under cathodic current load. Fig. 23 (b) shows the area specific resistance changes of the cell. During the 2200 h operation, no distinct degradation can be observed in the anode side, even when the Cr-source was introduced. However, in the cathode side, the polarization resistance  $R_p$  increases gradually within the 1400 h operation and elevates dramatically after introducing Cr-source.

An ordered structure such double perovskite is also a promising candidate for SOEC oxygen electrode. Tian et al. [126] investigated a double perovskite oxide  $PrBa_{0.5}Sr_{0.5}Co_{1.5}Fe_{0.5}O_{5+\delta}$  (PBSCF) as the oxygen electrode for reversible solid oxide electrochemical cells (RSOCs). In the SOEC mode, it displayed an electrolysis current density as high as 1.3 A/cm<sup>2</sup> when the temperature, absolute humidity and applied voltage were 800 °C, 50 vol% and 1.3 V, respectively.

The cells also exhibited excellent durability of 120 h in SOEC mode and presented good reversibility.

Zheng et al. [127] studied the electrochemical performance and the stability of  $SrBa_{0.75}Ca_{0.25}CoFeO_{5+\delta}$  (SBCCF), layered perovskite as the air electrode for SOECs. In a half-cell with three-electrode configuration, the initial polarization resistance,  $R_p$ , of GDC/SBCCF was 0.16  $\Omega$  cm<sup>2</sup> at 800 °C. Under an anodic polarization of 200 mV,  $R_p$  decreased to 0.03  $\Omega$  cm<sup>2</sup>; however, under the cathodic bias of 200 mV,  $R_p$  increased to 0.18  $\Omega$  cm<sup>2</sup>, indicating that SBCCF was more active towards OER than oxygen reduction reaction. During the electrolysis test under 1 A/cm<sup>2</sup> at 800 °C for 216 h,  $R_p$  of GDC/SBCCF increased to 0.52  $\Omega$  cm<sup>2</sup> in the first 96 h and remains at 0.52  $\Omega$  cm<sup>2</sup> for the remaining 120 h. In contrast,  $R_p$  of GDC/LSCF increased with a rate of 0.08  $\Omega$  cm<sup>2</sup>/100 h at the same time.

Although the intrinsic conductivity and catalytic ability of MIEC oxygen electrodes are sufficient for operations at high temperature and large current densities, their advantages are limited by the traditionally sponge-like structure because of the sluggish oxygen generation and release kinetics [128]. The poor oxygen release caused by tortuosity factors and low porosities and even blocked tunnels, would suffocate gas transport and subsequently cause anode delamination at high current densities [128].

Wu et al. [128] fabricated a novel honeycomb architecture anode to facilitate OER kinetics, whose merits in nature are the high mechanical strength, satisfactory tortuosity and large porosity. Fig. 24 shows the schematic illustration of the electrodes. In the actual operation, the honeycomb LSC/YSZ electrode (HE-LSC) showed the better and much more stable performance than the traditional LSC electrode (TE-LSC). As shown in Fig. 25, it was demonstrated that the traditional LSC showed negligible increases in  $R_p$  under a current density of 0.6 A/cm<sup>2</sup> for 1 h. But the electrolyzing voltage rapidly increased when the current density was increased to 1.2 A/cm<sup>2</sup> (blue line). In contrast, a three electrode cell with honeycomb architecture (27 wt% LSC loading) showed a stable operation with a current density of 1.5 A/cm<sup>2</sup> for 4 h, and no obvious performance degradation at 2.0 A/cm<sup>2</sup> for 6 h at 800 °C.

Khan et al. [129] reported a novel microstructure design by incorporation a porous YSZ layer between the LSM electrode and YSZ electrolyte to release this oxygen pressure. Symmetric cells with and without the porous YSZ layers were prepared and tested in air at 800 °C under the current densities of 0.5 and 1 A/cm<sup>2</sup> for 100 h. No delamination was observed for the samples with the porous YSZ layer, while the sample without the porous YSZ layer, the LSM was totally delaminated from the electrolyte just after 70 h, as shown in Fig. 26(a),(b) shows that for the traditional LSM, with the passage of time, more and more oxygen accumulate within the grain boundaries/pores of the electrolyte, until the LSM completely delaminates from the electrolyte. The improved performance for cells with porous YSZ is due to the shift of oxygen evolution reaction from the dense YSZ-LSM interface to a porous YSZ-LSM interface,

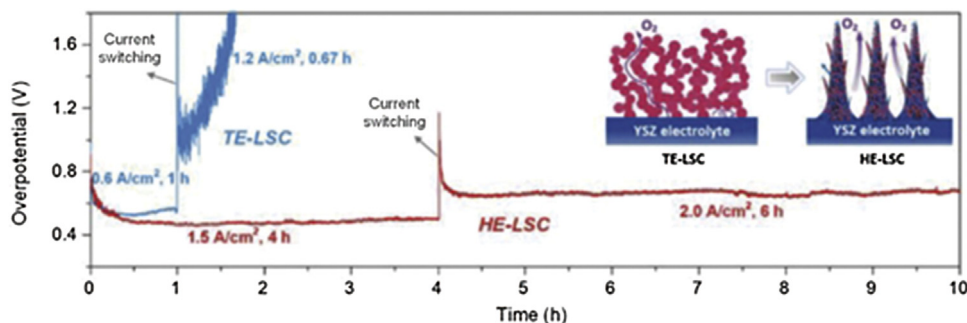


**Fig. 25.** [128] HE-LSC was measured in three-electrode mode at 1.5 A/cm<sup>2</sup> for 4 h and then at 2.0 A/cm<sup>2</sup> for 6 h at 800 °C, while TE-LSC measured in three-electrode mode at 0.6 A/cm<sup>2</sup> for 1 h and then at 1.2 A/cm<sup>2</sup> for 0.67 h at 800 °C. Reproduced with permission from ref [108]. Copyright 2018 John Wiley and Sons.

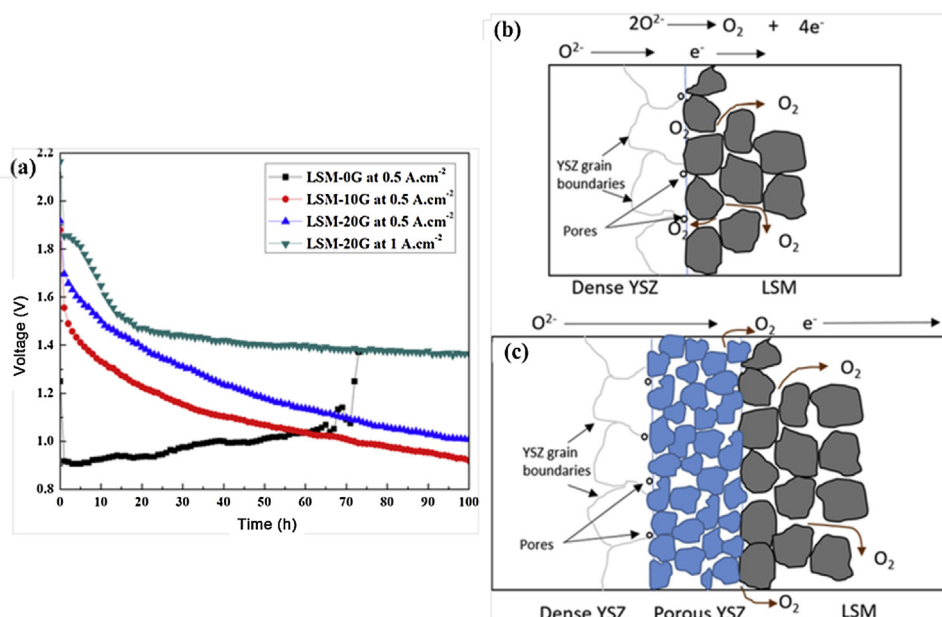


**Fig. 26.** [129] (a) The stability tests of LSM electrode with or without incorporation of porous YSZ layer: LSM-0G represents the traditional LSM electrode without porous YSZ; LSM-10G and LSM-20G are the cells with porous YSZ, but using different amounts of graphite to produce the porosity for the porous YSZ layer. (b) A possible illustration of the delamination of traditional LSM. (c) A possible mechanism of the ability of LSM-10G and LSM-20G to prevent delamination. Reproduced with permission from ref [130]. Copyright 2017 Elsevier, Inc.

as seen in Fig. 26(c). This shift also helps the oxygen to be easily released instead of going into the pores or grain boundaries of the electrolyte.

In recent years, interests in proton-conducting SOEC (H-SOEC) have been growing. One major advantage of H-SOEC is the low operation temperature, that is, 800 °C to 600 °C or even lower, because of its high ionic conductivity and low activation energy. Additionally, technical barriers, such as hydrogen separation and electrode instability due to Ni oxidation and oxygen electrode delamination, can be remarkably mitigated by the use of H-SOEC [130]. Wu et al. [130] fabricated a self-architected ultraporous 3D steam electrode developed for efficient H-SOECs below 600 °C. At 600 °C, the electrolysis current density reached 2.02 A/cm<sup>2</sup> at 1.6 V. Instead of fast degradation in most oxygen conducting SOECs, performance enhancement was observed during electrolysis at an applied voltage of 1.6 V at 500 °C for over 75 h, attributed to the “bridging” effect originating from reorganization of the steam electrode.

Li et al. [131] reported a high performing triple-conductive Pr<sub>2</sub>NiO<sub>4+δ</sub> anode for H-SOEC. Good chemical compatibility was verified between the PNO anode and BZCY electrolyte. Proton conduction was introduced most likely by water intake in the rock-salt layer. Excellent performance towards the water-splitting reaction was achieved on the PNO/BZCY composite anode, 0.52 Ω cm<sup>2</sup> for 550 °C, 0.057 Ω cm<sup>2</sup> for 700 °C. An electrolyzing current density of 977 mA/cm<sup>2</sup> was achieved at a potential of 1.3 V (0.37 V overpotential).

## 5. Concluding remarks

In this review, typical degradation phenomena of SOECs and the proposed mechanisms are summarized, in the aspects of anode (oxygen electrode), electrolyte and cathode (hydrogen or CO<sub>2</sub> electrode). Especial attention has been paid to the degradation in the anode side, such as anode delamination and electrolyte disintegration, with  $p_{O_2}$  as a major standpoint to understand critical degradation phenomena. Meanwhile, mechanistic works for examining the  $p_{O_2}$  distribution at electrode/electrolyte interfaces are presented, disclosing the different principles between SOEC and

SOFC to evaluate the faster degradation of SOEC than SOFC. At last, the newly presented counter strategies against the degradation of SOEC are also provided, including the novel infiltration and new anode materials as well as the microstructure improvement.

## Acknowledgements

This work is partially supported by U.S. Department of Energy under the contract number DE-EE0008378. We would like to thank the Technology Managers Drs. Eric Miller and David Peterson for the technical guidance and financial support.

## References

- [1] Y. Wang, T. Liu, L. Lei, F. Chen, *Fuel Process. Technol.* 161 (2017) 248–258.
- [2] M. Ni, M. Leung, D. Leung, *Int. J. Hydrogen Energy* 33 (2008) 2337–2354.
- [3] W. Li, N. Jiang, B. Hu, X. Liu, F. Song, G. Han, T.J. Jordan, T.B. Hanson, T.L. Liu, Y. Sun, *Chem.* 4 (2018) 637–649.
- [4] F. Song, W. Li, J. Yang, G. Han, P. Liao, Y. Sun, *Nat. Commun.* 9 (2018) 4531.
- [5] X. Zhang, Y. Song, G. Wang, X. Bao, *J. Energy Chem.* 26 (2017) 839–853.
- [6] Y. Zheng, J. Wang, B. Yu, W. Zhang, J. Chen, J. Qiao, J. Zhang, *Chem. Soc. Rev.* 46 (2017) 1427–1463.
- [7] W. Li, X. Gao, D. Xiong, F. Xia, J. Liu, W.-G. Song, J. Xu, S.M. Thalluri, M.F. Cerqueira, X. Fu, L. Liu, *Chem. Sci.* 8 (2017) 2952–2958.
- [8] W. Li, X. Gao, X. Wang, D. Xiong, P.-P. Huang, W.-G. Song, X. Bao, L. Liu, *J. Power Sources* 330 (2016) 156–166.
- [9] S.J. Kim, G.M. Choi, *Solid State Ion.* 262 (2014) 303–306.
- [10] T. Ogier, J.M. Bassat, F. Mauvy, S. Fourcade, J.C. Grenier, K. Couturier, M. Petitjean, J. Mougou, *Fuel Cells Wein.* (Weinh) 13 (2013) 536–541.
- [11] J. Schefold, A. Brisse, H. Poepke, *Int. J. Hydrogen Energy* 42 (2017) 13415–13426.
- [12] Y. Yan, Q. Fang, L. Blum, W. Lehnert, *Electrochim. Acta* 258 (2017) 1254–1261.
- [13] S.H. Jensen, P.H. Larsen, M. Mogensen, *Int. J. Hydrogen Energy* 32 (2007) 3253–3257.
- [14] G. Tao, K.R. Sridhar, C.L. Chan, *Solid State Ion.* 175 (2004) 621–624.
- [15] G. Tao, K.R. Sridhar, C.L. Chan, *Solid State Ion.* 175 (2004) 615–619.
- [16] K. Sridhar, B.T. Vaniman, *Solid State Ion.* 93 (1997) 321–328.
- [17] T. Yang, J. Liu, Y. Yu, Y.-L. Lee, H. Finklea, X. Liu, H.W. Abernathy, G.A. Hackett, *PCCP* 19 (2017) 30464–30472.
- [18] T. Yang, H. Sezer, I. Celik, H. Finklea, K. Gerdes, *Int. J. Electrochem. Sci.* 12 (2017) 6801–6828.
- [19] D.T. Whipple, P.J.A. Kenis, *J. Phys. Chem. Lett.* 1 (2010) 3451–3458.
- [20] C. Lamy, *Int. J. Hydrogen Energy* 41 (2016) 15415–15425.
- [21] X. Zhang, J.E. O'Brien, R.C. O'Brien, G.K. Housley, *J. Power Sources* 242 (2013) 566–574.

- [22] X. Zhang, J.E. O'Brien, R.C. O'Brien, J.J. Hartvigsen, G. Tao, G.K. Housley, *Int. J. Hydrogen Energy* 38 (2013) 20–28.
- [23] J. Schefold, A. Brisse, F. Tietz, *J. Electrochem. Soc.* 159 (2011) A137–A144.
- [24] J. Laurencin, M. Hubert, D.F. Sanchez, S. Pylypko, M. Morales, A. Morata, B. Morel, D. Montinaro, F. Lefebvre-Joud, E. Siebert, *Electrochim. Acta* 241 (2017) 459–476.
- [25] S.P. Jiang, *Asia-Pac. J. Chem. Eng.* 11 (2016) 386–391.
- [26] K. Chen, S.P. Jiang, *J. Electrochem. Soc.* 163 (2016) F3070–F3083.
- [27] P. Mocoteguy, A. Brisse, *Int. J. Hydrogen Energy* 38 (2013) 15887–15902.
- [28] R. Knibbe, M.L. Traulsen, A. Hauch, S.D. Ebbesen, M. Mogensen, *J. Electrochem. Soc.* 157 (2010) B1209.
- [29] K. Chen, S.P. Jiang, *Int. J. Hydrogen Energy* 36 (2011) 10541–10549.
- [30] J. Kim, H.-I. Ji, H.P. Dasari, D. Shin, H. Song, J.-H. Lee, B.-K. Kim, H.-J. Je, H.-W. Lee, K.J. Yoon, *Int. J. Hydrogen Energy* 38 (2013) 1225–1235.
- [31] M. Keane, M.K. Mahapatra, A. Verma, P. Singh, *Int. J. Hydrogen Energy* 37 (2012) 16776–16785.
- [32] J. Hwang, R.R. Rao, L. Giordano, Y. Katayama, Y. Yu, Y. Shao-Horn, *Science* 358 (2017) 751–756.
- [33] J. Stevenson, T. Armstrong, R. Carneim, L.R. Pederson, W. Weber, *J. Electrochem. Soc.* 143 (1996) 2722–2729.
- [34] C. Graves, S.D. Ebbesen, M. Mogensen, *Solid State Ion.* 192 (2011) 398–403.
- [35] R. Petri, E. Tang, T. Wood, C. Brown, M. Casteel, M. Pastula, M. Richards, 2016 Annual Progress Report II B 5, 2017, pp. 1–3.
- [36] A. Momma, T. Kato, Y. Kaga, S. Nagata, *J. Ceram. Soc. Jpn.* 105 (1997) 369–373.
- [37] M. Chen, Understanding the Thermodynamics at the LaMnO<sub>3</sub>–YSZ Interface in SOFC, 2005.
- [38] S.P. Jiang, *J. Solid State Electrochem.* 11 (2007) 93–102.
- [39] S. Jiang, W. Wang, *Electrochem. Solid-State Lett.* 8 (2005) A115–A118.
- [40] J. Mizusaki, Y. Yonemura, H. Kamata, K. Ohya, N. Mori, H. Takai, H. Tagawa, M. Dokiya, K. Naraya, T. Sasamoto, H. Inaba, T. Hashimoto, *Solid State Ion.* 132 (2000) 167–180.
- [41] D. Monceau, M. Filal, M. Tebtoub, C. Petot, G. Petot-Ervas, *Solid State Ion.* 73 (1994) 221–225.
- [42] M. Martin, *Solid State Ion.* 136–137 (2000) 331–337.
- [43] K. Chen, J. Hyodo, A. Dodd, N. Ai, T. Ishihara, L. Jian, S.P. Jiang, *Faraday Discuss.* 182 (2015) 457–476.
- [44] J.R. Mawdsley, J. David Carter, A. Jeremy Kropf, B. Yildiz, V.A. Maroni, *Int. J. Hydrogen Energy* 34 (2009) 4198–4207.
- [45] J. Bi, S. Yang, S. Zhong, J.-Q. Wang, C. Fan, X. Chen, Y. Liu, *J. Power Sources* 363 (2017) 470–479.
- [46] K. Chen, J. Hyodo, N. Ai, T. Ishihara, S.P. Jiang, *Int. J. Hydrogen Energy* 41 (2016) 1419–1431.
- [47] C.C. Wang, K. Chen, T. Jiang, Y. Yang, Y. Song, H. Meng, S.P. Jiang, B. Lin, *Electrochim. Acta* 269 (2018) 188–195.
- [48] J. Schefold, A. Brisse, H. Poepeke, *Electrochim. Acta* 179 (2015) 161–168.
- [49] D. The, S. Grieshammer, M. Schroeder, M. Martin, M. Al Daroukh, F. Tietz, J. Schefold, A. Brisse, *J. Power Sources* 275 (2015) 901–911.
- [50] M. Al Daroukh, F. Tietz, D. Sebold, H.P. Buchkremer, *Ionics* 21 (2014) 1039–1043.
- [51] F. Tietz, D. Sebold, A. Brisse, J. Schefold, *J. Power Sources* 223 (2013) 129–135.
- [52] J.C. De Vero, K. Develos-Bagarinao, H. Kishimoto, T. Ishiyama, K. Yamaji, T. Horita, H. Yokokawa, *J. Electrochem. Soc.* 163 (2016) F1463–F1470.
- [53] Z. Pan, Q. Liu, M. Ni, R. Lyu, P. Li, S.H. Chan, *Int. J. Hydrogen Energy* 43 (2018) 5437–5450.
- [54] A. Mahmoud, M. Al Daroukh, M. Lipinska-Chwalek, M. Luysberg, F. Tietz, R.P. Hermann, *Solid State Ion.* 312 (2017) 38–43.
- [55] C.E. Frey, Q. Fang, D. Sebold, L. Blum, N.H. Menzler, *J. Electrochem. Soc.* 165 (2018) F357–F364.
- [56] N. Ai, S. He, N. Li, Q. Zhang, W.D.A. Rickard, K. Chen, T. Zhang, S.P. Jiang, *J. Power Sources* 384 (2018) 125–135.
- [57] Z. He, L. Zhang, S. He, N. Ai, K. Chen, Y. Shao, S.P. Jiang, *J. Power Sources* 404 (2018) 73–80.
- [58] J.C. De Vero, K. Develos-Bagarinao, H. Matsuda, H. Kishimoto, T. Ishiyama, K. Yamaji, T. Horita, H. Yokokawa, *Solid State Ion.* 314 (2018) 165–171.
- [59] J.C. De Vero, K. Develos-Bagarinao, H. Kishimoto, T. Ishiyama, K. Yamaji, T. Horita, H. Yokokawa, *J. Electrochem. Soc.* 164 (2017) F259–F269.
- [60] B. Wei, K. Chen, L. Zhao, Z. Lü, S. Ping Jiang, *Phys. Chem. Chem. Phys.* 17 (2015) 1601–1609.
- [61] T. Kushi, *Int. J. Hydrogen Energy* 42 (2017) 9396–9405.
- [62] P. Kim-Lohsoontorn, D.J.L. Brett, N. Laosiripojana, Y.M. Kim, J.M. Bae, *Int. J. Hydrogen Energy* 35 (2010) 3958–3966.
- [63] C. Ferchaud, J.C. Grenier, Y. Zhang-Steenwinkel, M.M.A. van Tuel, F.P.F. van Berkel, J.M. Bassat, *J. Power Sources* 196 (2011) 1872–1879.
- [64] J.S.A. Carneiro, R.A. Brocca, M.L.R.S. Lucena, E. Nikolla, *Appl. Catal. B* 200 (2017) 106–113.
- [65] R.J. Woolley, S.J. Skinner, *Solid State Ion.* 255 (2014) 1–5.
- [66] A. Montenegro-Hernández, J. Vega-Castillo, L. Mogni, A. Caneiro, *Int. J. Hydrogen Energy* 36 (2011) 15704–15714.
- [67] J.D. Jorgensen, B. Dabrowski, S. Pei, D.R. Richards, D.G. Hinks, *Phys. Rev. B* 40 (1989) 2187–2199.
- [68] A. Flura, S. Dru, C. Nicollet, V. Vibhu, S. Fourcade, E. Lebraud, A. Rougier, J.M. Bassat, J.C. Grenier, *J. Solid State Chem.* 228 (2015) 189–198.
- [69] S.J. Kim, K.J. Kim, A.M. Dayaghi, G.M. Choi, *Int. J. Hydrogen Energy* 41 (2016) 14498–14506.
- [70] X. Tong, F. Zhou, S. Yang, S. Zhong, M. Wei, Y. Liu, *Ceram. Int.* 43 (2017) 10927–10933.
- [71] F. Chauveau, J. Mougín, F. Mauvy, J.-M. Bassat, J.-C. Grenier, *Int. J. Hydrogen Energy* 36 (2011) 7785–7790.
- [72] A. Egger, N. Schrödl, C. Gspan, W. Sitte, *Solid State Ion.* 299 (2017) 18–25.
- [73] G. Yang, C. Su, R. Ran, M.O. Tade, Z. Shao, *Energy Fuels* 28 (2013) 356–362.
- [74] T. Ogier, F. Mauvy, J.-M. Bassat, J. Laurencin, J. Mougín, J.-C. Grenier, *Int. J. Hydrogen Energy* 40 (2015) 15885–15892.
- [75] Y. Wang, T. Liu, S. Fang, F. Chen, *J. Power Sources* 305 (2016) 240–248.
- [76] B. Wei, J. Feng, L. Zhu, Z. Wang, X. Zhu, X. Huang, Y. Zhang, L. Xu, H. Gao, Z. Lü, *J. Eur. Ceram. Soc.* 38 (2018) 2396–2403.
- [77] M.A. Laguna-Bercero, *J. Power Sources* 203 (2012) 4–16.
- [78] K. Eguchi, T. Hatagishi, H. Arai, *Solid State Ion.* 86 (1996) 1245–1249.
- [79] S. Elangovan, J.J. Hartvigsen, L.J. Frost, *Int. J. Appl. Ceram. Technol.* 4 (2007) 109–118.
- [80] K. Huang, M. Feng, J.B. Goodenough, C. Milliken, *J. Electrochem. Soc.* 144 (1997) 3620–3624.
- [81] N. Maffei, G. de Silveira, *Solid State Ion.* 159 (2003) 209–216.
- [82] X. Zhang, S. Ohara, R. Maric, H. Okawa, T. Fukui, H. Yoshida, T. Inagaki, K. Miura, *Solid State Ion.* 133 (2000) 153–160.
- [83] S.D. Ebbesen, S.H. Jensen, A. Hauch, M.B. Mogensen, *Chem. Rev.* 114 (2014) 10697–10734.
- [84] M.A. Laguna-Bercero, R. Campana, A. Larrea, J.A. Kilner, V.M. Orera, *J. Power Sources* 196 (2011) 8942–8947.
- [85] A. Hauch, S.D. Ebbesen, S.H. Jensen, M. Mogensen, *J. Electrochem. Soc.* 155 (2008) B1184.
- [86] D.A. Osinkin, B.L. Kuzin, N.M. Bogdanovich, *Russ. J. Electrochem.* 46 (2010) 41–48.
- [87] Z. Jiao, N. Takagi, N. Shikazono, N. Kasagi, *J. Power Sources* 196 (2011) 1019–1029.
- [88] L. Holzer, B. Iwanschitz, T. Hocker, B. Münch, M. Prestat, D. Wiedenmann, U. Vogt, P. Holtappels, J. Sfeir, A. Mai, T. Graule, *J. Power Sources* 196 (2011) 1279–1294.
- [89] S.-D. Kim, D.-W. Seo, A.K. Dorai, S.-K. Woo, *Int. J. Hydrogen Energy* 38 (2013) 6569–6576.
- [90] T. Matsui, R. Kishida, J.-Y. Kim, H. Muroyama, K. Eguchi, *J. Electrochem. Soc.* 157 (2010) B776–B781.
- [91] A. Hauch, Sr.Hj. Jensen, Jr.B. Bilde-Soerensen, M. Mogensen, *J. Electrochem. Soc.* 154 (2007) A619.
- [92] C. Chatzichristodoulou, M. Chen, P.V. Hendriksen, T. Jacobsen, M.B. Mogensen, *Electrochim. Acta* 189 (2016) 265–282.
- [93] M. Gong, X. Liu, J. Tremblay, C. Johnson, *J. Power Sources* 168 (2007) 289–298.
- [94] S.D. Ebbesen, M. Mogensen, *Electrochem. Solid-State Lett.* 13 (2010) B106–B108.
- [95] S.D. Ebbesen, M. Mogensen, *J. Power Sources* 193 (2009) 349–358.
- [96] S.D. Ebbesen, C. Graves, A. Hauch, Sr.H. Jensen, M. Mogensen, *J. Electrochem. Soc.* 157 (2010) B1419.
- [97] S. Wang, H. Tsuruta, M. Asanuma, T. Ishihara, *Adv. Energy Mater.* 5 (2015), 1401003.
- [98] S. Wang, A. Inoishi, J.-e. Hong, Y.-w. Ju, H. Hagiwara, S. Ida, T. Ishihara, *J. Mater. Chem. A Mater. Energy Sustain.* 1 (2013) 12455.
- [99] S. Liu, Q. Liu, J.-L. Luo, *ACS Catal.* 6 (2016) 6219–6228.
- [100] Y. Zhou, Z. Zhou, Y. Song, X. Zhang, F. Guan, H. Lv, Q. Liu, S. Miao, G. Wang, X. Bao, *Nano Energy* 50 (2018) 43–51.
- [101] D. Kondepudi, I. Prigogine, *Modern Thermodynamics: From Heat Engines to Dissipative Structures*, John Wiley & Sons, 2014.
- [102] A.V. Virkar, *J. Power Sources* 147 (2005) 8–31.
- [103] A.V. Virkar, *J. Electrochem. Soc.* 138 (1991) 1481.
- [104] H.-T. Lim, A.V. Virkar, *J. Power Sources* 192 (2009) 267–278.
- [105] H.-T. Lim, A.V. Virkar, *J. Power Sources* 180 (2008) 92–102.
- [106] A.V. Virkar, *J. Power Sources* 172 (2007) 713–724.
- [107] A.V. Virkar, *Int. J. Hydrogen Energy* 35 (2010) 9527–9543.
- [108] A.V. Virkar, J. Nachlas, A.V. Joshi, J. Diamond, *J. Am. Ceram. Soc.* 73 (1990) 3382–3390.
- [109] H.-T. Lim, A.V. Virkar, *J. Power Sources* 185 (2008) 790–800.
- [110] T. Jacobsen, M. Mogensen, *ECS Trans.* 13 (2008) 259–273.
- [111] A. Mineshige, T. Taji, Y. Muroi, M. Kobune, S. Fujii, N. Nishi, M. Inaba, Z. Ogumi, *Solid State Ion.* 135 (2000) 481–485.
- [112] S.N. Rashkeev, M.V. Glazoff, *Int. J. Hydrogen Energy* 37 (2012) 1280–1291.
- [113] T. Yang, I.B. Celik, S. Lee, W.K. Epting, R. Mahbub, T. Hsu, P.A. Salvador, H.W. Abernathy, G.A. Hackett, *Int. J. Hydrogen Energy* 43 (2018) 15445–15456.
- [114] H. Sezer, I.B. Celik, T. Yang, *ECS Trans.* 68 (2015) 2515–2525.
- [115] J. Liu, Y. Yu, T. Yang, O. Ozmen, H. Finklea, E.M. Sabolsky, H. Abernathy, P.R. Ohodnicki, G.A. Hackett, *ECS Trans.* 78 (2017) 689–699.
- [116] T. Yang, I.B. Celik, H. Sezer, S. Lee, K. Gerdes, *ECS Trans.* 66 (2015) 137–142.
- [117] T. Yang, J. Liu, H.O. Finklea, H. Abernathy, G.A. Hackett, *ECS Trans.* 78 (2017) 2699–2709.
- [118] T. Yang, H. Sezer, I.B. Celik, H.O. Finklea, K. Gerdes, *ECS Trans.* 68 (2015) 2397–2411.
- [119] K. Chen, N. Ai, S.P. Jiang, *Electrochem. Commun.* 19 (2012) 119–122.
- [120] K. Chen, N. Ai, S.P. Jiang, *Int. J. Hydrogen Energy* 39 (2014) 10349–10358.
- [121] Y. Song, X. Zhang, Y. Zhou, Q. Jiang, F. Guan, H. Lv, G. Wang, X. Bao, *Energy Storage Mater.* 13 (2018) 207–214.
- [122] H. Zheng, Y. Tian, L. Zhang, B. Chi, J. Pu, L. Jian, *J. Power Sources* 383 (2018) 93–101.



- [123] W. Li, B. Guan, X. Zhang, J. Yan, Y. Zhou, X. Liu, PCCP 18 (2016) 8502–8511.
- [124] W. Li, B. Guan, J. Yan, N. Zhang, X. Zhang, X. Liu, J. Power Sources 318 (2016) 178–183.
- [125] B. Guan, W. Li, X. Zhang, X. Liu, ECS Trans. 68 (2015) 801–808.
- [126] Y. Tian, J. Li, Y. Liu, J. Yang, B. Liu, L. Jia, J. Jiang, B. Chi, J. Pu, J. Li, Int. J. Hydrogen Energy 43 (2018) 12603–12609.
- [127] Y. Zheng, H. Yang, Z. Pan, C. Zhang, Electrochim. Acta 251 (2017) 581–587.
- [128] T. Wu, W. Zhang, Y. Li, Y. Zheng, B. Yu, J. Chen, X. Sun, Adv. Energy Mater. 8 (2018), 1802203.
- [129] M.S. Khan, X. Xu, J. Zhao, R. Knibbe, Z. Zhu, J. Power Sources 359 (2017) 104–110.
- [130] W. Wu, H. Ding, Y. Zhang, Y. Ding, P. Katiyar, P.K. Majumdar, T. He, D. Ding, Adv. Sci. 5 (2018), 1800360.
- [131] W. Li, B. Guan, L. Ma, S. Hu, N. Zhang, X. Liu, J. Mater. Chem. A Mater. Energy Sustain. 6 (2018) 18057–18066.
- [132] A. Mitterdorfer, L.J. Gauckler, Solid State Ion. 111 (1998) 185–218.
- [133] C. Clausen, C. Bagger, J.B. Bilde-Sørensen, A. Horsewell, Solid State Ion. 70–71 (1994) 59–64.